International Journal of Heat and Mass Transfer 78 (2014) 670–687

Contents lists available at ScienceDirect

International Journal of Heat and Mass Transfer

journal homepage: www.elsevier.com/locate/ijhmt

Numerical modeling of the non-isothermal liquid droplet impact on a hot solid substrate

Sashikumaar Ganesan [a,*], Sangeetha Rajasekaran [a], Lutz Tobiska [b]

[a] Numerical Mathematics and Scientific Computing, SERC, Indian Institute of Science, Bangalore 560 012, India
[b] Institute of Analysis and Numerical Computation, OvG University, PF4120, 39016 Magdeburg, Germany

ARTICLE INFO

Article history:
Received 11 November 2013
Received in revised form 12 June 2014
Accepted 8 July 2014

Keywords:
Finite elements
ALE approach
Moving mesh
Impinging droplets
Moving contact line
Dynamic contact angle
Heat transfer

ABSTRACT

The heat transfer from a solid phase to an impinging non-isothermal liquid droplet is studied numerically. A new approach based on an arbitrary Lagrangian–Eulerian (ALE) finite element method for solving the incompressible Navier–Stokes equations in the liquid and the energy equation within the solid and the liquid is presented. The novelty of the method consists in using the ALE-formulation also in the solid phase to guarantee matching grids along the liquid–solid interface. Moreover, a new technique is developed to compute the heat flux without differentiating the numerical solution. The free surface and the liquid–solid interface of the droplet are represented by a moving mesh which can handle jumps in the material parameter and a temperature dependent surface tension. Further, the application of the Laplace–Beltrami operator technique for the curvature approximation allows a natural inclusion of the contact angle. Numerical simulation for varying Reynold, Weber, Peclét and Biot numbers are performed to demonstrate the capabilities of the new approach.

1. Introduction

The interaction between sprays and hot solid objects occur in a wide variety of industrial and environmental applications. Nevertheless, our understanding of the mechanisms involved in the process is far from being complete. Therefore, the study of the hydrodynamic and thermodynamic behavior of a single droplet impinging on a solid substrate is of fundamental importance.

As a droplet nears a hot solid substrate, heat is transferred from the solid to the liquid phase by conduction, convection and radiation. This energy is used to increase the temperature of the liquid or to vaporize the liquid from the base of the droplet. In the latter case a direct contact between the solid and the liquid phase is excluded (Leidenfrost phenomenon). For a surface temperature below the Leidenfrost temperature we suppose that the direct liquid-wall contact and the kinetic of the droplet spreading dominate the heat transfer. Thus, we consider in this paper the coupled heat transfer process in a single deforming droplet and in the solid phase during the spreading and recoiling from the moment of its impact till losing a direct contact with the solid. Despite several advances made in the field of Computational Fluid Dynamics, modeling and simulation of these processes are still very challenging. The Volume-of-Fluid [1–5], Level set [6–10], Immersed Boundary/Front Tracking [11–15] and the arbitrary Lagrangian Eulerian [16–21] are the most commonly used methods for tracking/capturing moving interfaces/boundaries.

Although several interface capturing/tracking methods have been proposed in the literature, only a few numerical studies incorporated the thermodynamic behavior. In the early study [22], MAC-type solution technique has been used for the computations of a water droplet impinging on a flat surface above the Leidenfrost temperature. However, the unsteady heat transfer computation has been neglected in this study. A considerable number of numerical simulations using the Volume-of-Fluid method have been reported in the literature for droplets impinging on a hot surface [23–29]. Also, numerical studies using the Level set method [30,31] and the Immersed Boundary method [32,33] have been reported in the literature. All these methods can be classified as fixed grid (Eulerian) methods. Computations using the Lagrangian approach for a liquid droplet impinging on a hot solid substrate have been presented in [34]. To the best of the authors knowledge, computations of a liquid droplet impinging on a hot solid substrate using the arbitrary Lagrangian–Eulerian (ALE) approach in both phases have not been reported in the literature.

In this paper, we present an accurate and efficient sharp interface ALE finite element approach for the computation of a non-isothermal liquid droplet impinging on a hot solid substrate. The Marangoni force, the surface force, and the jumps in the material

* Corresponding author.
E-mail addresses: sashi@serc.iisc.in (S. Ganesan), sangeetha@nmsc.serc.iisc.ernet.in (S. Rajasekaran), tobiska@ovgu.de (L. Tobiska).

http://dx.doi.org/10.1016/j.ijheatmasstransfer.2014.07.019
0017-9310/

parameters are incorporated into the model very accurately since the free surface and the liquid–solid interface are resolved by the computational mesh in the ALE approach. Also, spurious velocities arising often in other methods can be suppressed by using this approach [35]. Further, we use the Laplace–Beltrami operator technique [36,37] to treat the curvature in a semi-implicit manner [38]. This technique allows us to include the equilibrium contact angle into the model weakly [39]. Since the moving liquid–solid interface is resolved by the computational mesh, the energy equation in both the liquid and the solid phases can be solved by a one-field formulation. This allows us also to develop a new technique for computing the heat flux from the solid phase to the liquid phase without differentiating the numerical solution.

The paper is organized as follows. In Section 2 we introduce the governing equations for the fluid flow and the heat transfer in the liquid and solid phases. Then, the complex coupled problem is formulated in dimensionless quantities. Section 3 is devoted to the ingredients of our numerical approach. First, we explain in detail how the curvature approximation by the Laplace–Beltrami technique and the contact angle condition can be implemented in the weak form of the Navier–Stokes equations. We derive a one-field formulation for the temperature in the liquid–solid domain. Next the ALE approach to handle the moving mesh is discussed. Then, under the assumption of axisymmetry, the fully weak 3D formulation is transferred to the weak axisymmetric formulation. The discretization in space and time, in particular, the semi-discretization of the curvature term are given. Finally, we address the mesh handling techniques at the liquid–solid interface and the inner mesh update. Section 4 is concerned with numerical tests for varying Reynolds, Weber, Peclét and Biot numbers showing the capabilities of the new method. We shortly summarize the proposed numerical method and the obtained results in Section 5.

2. Mathematical model

2.1. Governing equations for the fluid flow

We consider a liquid droplet impinging on a horizontal hot substrate, see Fig. 1. The fluid is assumed to be incompressible; density and viscosity are constant. The governing equations for the fluid flow describing the sequence of spreading and recoiling of an impinging droplet in the given time interval (0, I) are the time-dependent incompressible Navier–Stokes equations

$$\frac{\partial \mathbf{u}}{\partial t} + (\mathbf{u}\cdot\nabla)\mathbf{u} - \frac{1}{\rho}\nabla\cdot(\mathbb{T}(\mathbf{u},p)) = g\mathbf{e} \quad \text{in } \Omega_F(t)\times(0,\mathrm{I}), \tag{1}$$

$$\nabla\cdot\mathbf{u} = 0 \quad \text{in } \Omega_F(t)\times(0,\mathrm{I}), \tag{2}$$

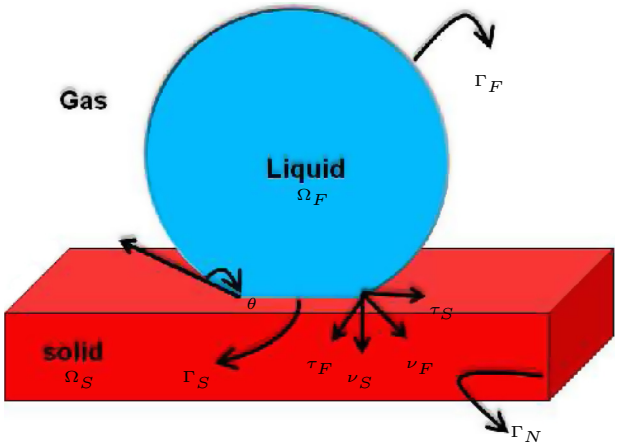

Fig. 1. Computational model for an impinging droplet on a hot solid substrate.

with the initial condition

$$\mathbf{u}(\cdot,0) = \mathbf{u}_0 \quad \text{in } \Omega_F(0) \tag{3}$$

and the boundary conditions given below. The time-dependent domain of the deforming droplet is denoted by $\Omega_F(t)$. The set $\Omega_F(t)\times(0,I)$ is understood as $\{(x,t)\in\mathbb{R}^4 : t\in(0,I), x\in\Omega_F(t)\}$. The boundary of the droplet satisfies $\partial\Omega_F(t) = \Gamma_F(t)\cup\Gamma_S(t)$, where $\Gamma_F(t)$ and $\Gamma_S(t)$ are the free surface and the liquid–solid interface of the droplet, respectively. Further, $\mathbf{u}$ is the velocity, p is the pressure, ρ is the density, g is the gravitational constant, t is the time, $\mathbf{e}$ is an unit vector in the opposite direction of the gravitational force, $\mathbf{u}_0(0,0,-u_{imp})$ is a given initial velocity and I is a given final time. The stress tensor $\mathbb{T}(\mathbf{u},p)$ for a Newtonian incompressible fluid is given by

$$\mathbb{T}(\mathbf{u},p) := 2\mu\mathbb{D}(\mathbf{u}) - p\mathbb{I}, \quad \mathbb{D}(\mathbf{u})_{ij} = \frac{1}{2}\left(\frac{\partial u_i}{\partial x_j} + \frac{\partial u_j}{\partial x_i}\right),$$

with $i,j = 1,\dots,3$, where μ denotes the dynamic viscosity, $\mathbb{D}(\mathbf{u})$ the velocity deformation tensor and $\mathbb{I}$ the identity tensor. The kinematic and force balancing conditions on the free surface Γ_F are given by

$$\mathbf{u}\cdot\boldsymbol{\nu}_F = \mathbf{w}\cdot\boldsymbol{\nu}_F \quad \text{on } \Gamma_F(t), \tag{4}$$

$$\mathbb{T}(\mathbf{u},p)\cdot\boldsymbol{\nu}_F = \sigma(T_F)\mathcal{K}\boldsymbol{\nu}_F + \underline{\nabla}\sigma(T_F) \quad \text{on } \Gamma_F(t). \tag{5}$$

Here, $\boldsymbol{\nu}_F$ denotes the unit outer normal vector on the free surface, $\mathcal{K}$ denotes the sum of the principal curvatures, $\underline{\nabla}$ the tangential gradient (defined in Section 3.1), $\mathbf{w}$ the velocity of the computational domain $\Omega_F(t), T_F$ the temperature on $\Gamma_F(t), \sigma(T_F)$ the temperature-dependent surface tension. Let $\boldsymbol{\tau}_{i,F}, i = 1,2$, denote tangential vectors on the free surface Γ_F(t). Then, (5) is equivalent to

$$\boldsymbol{\nu}_F\cdot\mathbb{T}(\mathbf{u},p)\cdot\boldsymbol{\nu}_F = \sigma(T_F)\mathcal{K}, \quad \text{on } \Gamma_F(t),$$
$$\boldsymbol{\tau}_{i,F}\cdot\mathbb{T}(\mathbf{u},p)\cdot\boldsymbol{\nu}_F = \boldsymbol{\tau}_{i,F}\cdot\nabla\sigma(T_F) \quad \text{on } \Gamma_F(t),$$

since the tangential gradient on $\Gamma_F(t)$ is perpendicular to $\boldsymbol{\nu}_F$. Further, for simplicity we assume that the temperature-dependent surface tension $\sigma(T_F)$ follows a simple linear law

$$\sigma(T_F) = \sigma_{ref} - \mathcal{C}_1(T_F - T_{ref}), \tag{6}$$

where T_{ref} is some reference temperature, σ_{ref} is the surface tension coefficient at the reference temperature and $\mathcal{C}_1 > 0$ is the negative rate of change of surface tension with temperature. The changes in the local surface temperature $T_F$on the free surface induce variations in the surface tension. Due to these variations in the surface tension, the fluid moves away from the region of low surface tension to the region of high surface tension. This effect is called Marangoni convection. Note that for large T_F the surface tension (6) could become negative and the model would be no longer correct. In order to avoid this unphysical behavior we check in our numerical computations whether the computed surface tension values are in the range of validity of the law (6).

Next, for moving contact line problems the conventional no-slip boundary condition at fixed walls cannot be used along the solid surface. Imposing the no-slip boundary condition at the moving contact line, where the free surface and the liquid–solid interface meet, leads to an non-integrable force singularity at the contact line [40–43]. Therefore, we use instead the Navier–slip boundary condition [39,44–46] on the liquid–solid interface $\Gamma_S(t)$

$$\mathbf{u}\cdot\boldsymbol{\nu}_S = 0, \quad \mathbf{u}\cdot\boldsymbol{\tau}_{i,S} + \epsilon_\mu(\boldsymbol{\tau}_{i,S}\cdot\mathbb{T}(\mathbf{u},p)\cdot\boldsymbol{\nu}_S) = 0. \tag{7}$$

Here, $\boldsymbol{\nu}_S$ and $\boldsymbol{\tau}_{i,S}, i = 1,2$ denote the outer unit normal and tangential vectors on the liquid–solid interface. Further, ϵ_μ is the slip coefficient [39,47].

2.2. Heat transfer from the solid into the liquid phase

The heat transfer in the moving droplet and in the fixed solid phase are described by the energy equation. In this study, we

assume that the material properties such as densities, thermal conductivities and specific heats are constant in the liquid and the solid phases, respectively. The solid phase will be denoted by Ω_S and is fixed over time. However, due to the changing wetting area $\Gamma_S(t)$ the non-wetted part $\Gamma_N(t) := \partial\Omega_S \setminus \Gamma_S(t)$ of the boundary along which we describe Neumann type boundary conditions becomes time-dependent. The heat transfer in the liquid and solid phase, respectively, is described by the energy equations

$$\frac{\partial T_F}{\partial t} + \mathbf{u}\cdot\nabla T_F = \frac{\lambda_F}{c_p^F\rho}\Delta T_F \quad \text{in } \Omega_F(t)\times(0,\mathrm{I}), \tag{8}$$

$$\frac{\partial T_S}{\partial t} = \frac{\lambda_S}{c_p^S\rho_S}\Delta T_S \quad \text{in } \Omega_S\times(0,\mathrm{I}). \tag{9}$$

We complete (8) and (9) by the initial conditions

$$T_F(\cdot,0) = T_{F,0} \text{ in } \Omega_F(0), \quad T_S(\cdot,0) = T_{S,0} \text{ in } \Omega_S, \tag{10}$$

the boundary conditions at the free surface $\Gamma_F(t)$ and along the non-wetting part of the solid $\Gamma_N(t)$

$$-\lambda_F\frac{\partial T_F}{\partial \boldsymbol{\nu}_F} = \alpha_F(T_F - T_\infty) \text{ on } \Gamma_F(t), \quad \frac{\partial T_S}{\partial n} = 0 \text{ on } \Gamma_N(t) \tag{11}$$

and the transition conditions (continuity of temperature and heat flux)

$$\lambda_F\frac{\partial T_F}{\partial \boldsymbol{\nu}_F} = -\lambda_S\frac{\partial T_S}{\partial \boldsymbol{\nu}_S}, \quad T_F = T_S \text{ on } \Gamma_S(t). \tag{12}$$

Here, T_F and T_S are the temperatures in $\Omega_F(t)$ and Ω_S, respectively, λ_F, λ_S the conductivities, ρ, ρ_S the densities, c_p^F, c_p^S the specific heat of the fluid and the solid. Finally, T_∞ denotes the temperature of the surrounding gas, α_F is the convection heat transfer coefficient on the liquid–gas interface, and n is the outer normal on $\Gamma_N(t)$.

2.3. Dimensionless form of the model equations

In this section we derive the dimensionless form of the coupled Navier–Stokes and energy equations. We introduce the scaling factors L and U as characteristic length and velocity, respectively. Furthermore, we define the dimensionless variables

$$\tilde{x} = \frac{x}{L}, \quad \tilde{\mathbf{u}} = \frac{\mathbf{u}}{U}, \quad \tilde{\mathbf{w}} = \frac{\mathbf{w}}{U}, \quad \tilde{t} = \frac{tU}{L}, \quad \tilde{\mathrm{I}} = \frac{\mathrm{I}U}{L}, \quad \tilde{p} = \frac{p}{\rho U^2}$$

and the dimensionless numbers (Reynolds, Weber, Froude and slip, respectively)

$$\mathrm{Re} = \frac{\rho UL}{\mu}, \quad \mathrm{We} = \frac{\rho U^2 L}{\sigma_{ref}}, \quad \mathrm{Fr} = \frac{U^2}{Lg}, \quad \beta_\epsilon = \epsilon_\mu \rho U.$$

We introduce a dimensionless stress tensor $\mathbb{S}(\tilde{\mathbf{u}},\tilde{p})$ by

$$\mathbb{S}(\tilde{\mathbf{u}},\tilde{p}) = \frac{1}{\rho U^2}\mathbb{T}(\tilde{\mathbf{u}},\tilde{p}) = \left(\frac{1}{\mathrm{Re}}\left(\frac{\partial\tilde{u}_i}{\partial\tilde{x}_j} + \frac{\partial\tilde{u}_j}{\partial\tilde{x}_i}\right) - p\delta_{ij}\right)_{i,j=1,\dots,3}$$

and the dimensionless temperature in the liquid phase

$$\widetilde{T}_F = \frac{T_F - T_\infty}{T_{ref} - T_\infty}.$$

Writing the coupled system in the new dimensionless variables and omitting the tilde afterwards we end up with the dimensionless Navier–Stokes problem

$$\frac{\partial\mathbf{u}}{\partial t} + (\mathbf{u}\cdot\nabla)\mathbf{u} - \nabla\cdot\mathbb{S}(\mathbf{u},p) = \frac{1}{\mathrm{Fr}}\mathbf{e} \quad \text{in } \Omega_F(t)\times(0,\mathrm{I}), \tag{13}$$

$$\nabla\cdot\mathbf{u} = 0 \quad \text{in } \Omega_F(t)\times(0,\mathrm{I}), \tag{14}$$

$$\mathbf{u}\cdot\boldsymbol{\nu}_S = 0 \quad \text{on } \Gamma_S(t)\times(0,\mathrm{I}), \tag{15}$$

$$\beta_\epsilon(\boldsymbol{\tau}_{i,S}\cdot\mathbb{S}(\mathbf{u},p)\cdot\boldsymbol{\nu}_S) = -\mathbf{u}\cdot\boldsymbol{\tau}_{i,S} \quad \text{on } \Gamma_S(t)\times(0,\mathrm{I}), \tag{16}$$

$$\mathbf{u}\cdot\boldsymbol{\nu}_F = \mathbf{w}\cdot\boldsymbol{\nu}_F \quad \text{on } \Gamma_F(t)\times(0,\mathrm{I}), \tag{17}$$

with the initial condition

$$\mathbf{u}(\cdot,0) = \mathbf{u}_0/U.$$

The dimensionless form of the normal stress boundary condition on Γ_F becomes

$$\boldsymbol{\nu}_F\cdot\mathbb{S}(u,p)\cdot\boldsymbol{\nu}_F = \frac{1}{\mathrm{We}}(1 - \mathcal{C}_0(T_F - 1))\mathcal{K} \tag{18}$$

and the shear stress boundary condition reads

$$\boldsymbol{\tau}_{i,F}\cdot\mathbb{S}(u,p)\cdot\boldsymbol{\nu}_F = -\frac{\mathcal{C}_0}{\mathrm{We}}\boldsymbol{\tau}_{i,F}\cdot\nabla T_F, \tag{19}$$

where

$$\mathcal{C}_0 = \frac{\mathcal{C}_1}{\sigma_{ref}(T_{ref} - T_\infty)}.$$

In order to write the energy equations in a dimensionless form, we define in addition the dimensionless temperature in the solid phase as

$$\widetilde{T}_S = \frac{T_S - T_\infty}{T_{ref} - T_\infty}.$$

After transforming the energy equations as well as the initial, boundary and transition conditions in dimensionless form we omit the tilde and obtain the dimensionless energy equations in the liquid and solid phase

$$\frac{\partial T_F}{\partial t} + \mathbf{u}\cdot\nabla T_F - \frac{1}{\mathrm{Pe_F}}\Delta T_F = 0 \quad \text{in } \Omega_F(t)\times(0,\mathrm{I}), \tag{20}$$

$$\frac{\partial T_S}{\partial t} - \frac{1}{\mathrm{Pe_S}}\Delta T_S = 0 \quad \text{in } \Omega_S\times(0,\mathrm{I}), \tag{21}$$

respectively. The dimensionless initial conditions become

$$T_F(\cdot,0) = \frac{T_{F,0} - T_\infty}{T_{ref} - T_\infty} \text{ in } \Omega_F(0), \tag{22}$$

$$T_S(\cdot,0) = \frac{T_{S,0} - T_\infty}{T_{ref} - T_\infty} \text{ in } \Omega_S. \tag{23}$$

Finally, the dimensionless thermal boundary and transition conditions can be written as

$$-\frac{\partial T_F}{\partial \boldsymbol{\nu}_F} = \mathrm{Bi}T_F \quad \text{on } \Gamma_F(t)\times(0,\mathrm{I}), \tag{24}$$

$$\frac{\partial T_F}{\partial \boldsymbol{\nu}_F} = -\frac{\lambda_S}{\lambda_F}\frac{\partial T_S}{\partial \boldsymbol{\nu}_S} \quad \text{on } \Gamma_S(t)\times(0,\mathrm{I}), \tag{25}$$

$$T_F = T_S \quad \text{on } \Gamma_S(t)\times(0,\mathrm{I}), \tag{26}$$

$$\frac{\partial T_S}{\partial \boldsymbol{n}} = 0 \quad \text{on } \Gamma_N(t)\times(0,\mathrm{I}). \tag{27}$$

In the above equations, $\mathrm{Pe}_F, \mathrm{Pe}_S$, and Bi denote the dimensionless Peclet numbers in the fluid and solid, respectively, and Biot number, given by

$$\mathrm{Pe}_F = \frac{LUc_p^F\rho}{\lambda_F}, \quad \mathrm{Pe}_S = \frac{LUc_p^S\rho_S}{\lambda_S}, \quad \mathrm{Bi} = \frac{\alpha_F L}{\lambda_F}.$$

3. Numerical scheme

We start with the weak form of the Navier–Stokes equations and derive a weak one-field formulation of the energy equation. Next, we describe the arbitrary Langrangian–Eulerian approach to handle the equations on time-dependent domains. Then the discretization in space and time will be given. Finally in this section, we discuss aspects of the mesh handling at the time-dependent liquid–solid interface and within the domains $\Omega_F(t)$ and Ω_S.

3.1. Weak form of the Navier–Stokes equations

We use the standard notations L^2, H^1 and $(\cdot,\cdot)_\omega$ for Sobolev spaces and the inner product in $L^2(\omega)$ and its vector-valued versions, respectively. We look for velocity and pressure in the spaces

$$V := \{\mathbf{v} \in H^1(\Omega_F(t))^3 : \mathbf{v}\cdot\boldsymbol{\nu}_S = 0 \text{ on } \Gamma_S(t)\}, \tag{28}$$

$$Q := L^2(\Omega_F(t)), \tag{29}$$

thus the no penetration boundary condition $\mathbf{u}\cdot\boldsymbol{\nu}_S = 0$ on liquid–solid interface $\Gamma_S(t)$ will be implemented in both the ansatz and test velocity spaces. Multiplying the momentum and mass balance equations. (13) and (14) by test functions $\mathbf{v} \in V$ and $q \in Q$ respectively, integrating over $\Omega_F(t)$ and applying the Gaussian theorem for the part including the stress tensor lead us to the weak formulation. In particular, the term including the symmetric stress tensor can be written as

$$\begin{aligned}
&-\int_{\Omega_F} \nabla\cdot\mathbb{S}(\mathbf{u},p)\cdot\mathbf{v}dx + \int_{\partial\Omega_F} \mathbf{v}\cdot\mathbb{S}(\mathbf{u},p)\cdot\boldsymbol{\nu}d\gamma \\
&= \int_{\Omega_F} \mathbb{S}(\mathbf{u},p):\nabla\mathbf{v}dx = \int_{\Omega_F}\frac{1}{2}\mathbb{S}(\mathbf{u},p):\nabla\mathbf{v}dx + \int_{\Omega_F}\frac{1}{2}\mathbb{S}^T(\mathbf{u},p):\nabla\mathbf{v}dx \\
&= \frac{2}{\mathrm{Re}}\int_{\Omega_F}\mathbb{D}(\mathbf{u}):\mathbb{D}(\mathbf{v})dx - \int_{\Omega_F} p\nabla\cdot\mathbf{v}dx.
\end{aligned} \tag{30}$$

Now, the free surface and liquid–solid boundary conditions will be included in the weak form as follows. We move the boundary integral term in (30) to the right hand side and split it into integrals over Γ_S and Γ_F

$$\begin{aligned}
&-\int_{\partial\Omega_F}\mathbf{v}\cdot\mathbb{S}(\mathbf{u},p)\cdot\boldsymbol{\nu}d\gamma = -\int_{\Gamma_S}\mathbf{v}\cdot\mathbb{S}(\mathbf{u},p)\cdot\boldsymbol{\nu}_S d\gamma_S \\
&-\int_{\Gamma_F}\mathbf{v}\cdot\mathbb{S}(\mathbf{u},p)\cdot\boldsymbol{\nu}_F d\gamma_F.
\end{aligned} \tag{31}$$

Then, using the orthonormal decomposition

$$\mathbf{v} = (\mathbf{v}\cdot\boldsymbol{\nu}_S)\boldsymbol{\nu}_S + \sum_{i=1}^{2}(\mathbf{v}\cdot\boldsymbol{\tau}_{i,S})\boldsymbol{\tau}_{i,S} \quad \text{on } \Gamma_S,$$

the no penetration condition (15) incorporated in (28) and the slip with friction boundary condition (16), the integral over the liquid–solid interface can be written as

$$\begin{aligned}
-\int_{\Gamma_S}\mathbf{v}\cdot\mathbb{S}(\mathbf{u},p)\cdot\boldsymbol{\nu}_S d\gamma_S &= -\sum_{i=1}^{2}\int_{\Gamma_S}(\mathbf{v}\cdot\boldsymbol{\tau}_{i,S})\boldsymbol{\tau}_{i,S}\cdot\mathbb{S}(\mathbf{u},p)\cdot\boldsymbol{\nu}_S d\gamma_S \\
&= \frac{1}{\beta_\epsilon}\sum_{i=1}^{2}\int_{\Gamma_S}(\mathbf{u}\cdot\boldsymbol{\tau}_{i,S})(\mathbf{v}\cdot\boldsymbol{\tau}_{i,S})d\gamma_S.
\end{aligned} \tag{32}$$

Similarly, using the orthonormal decomposition

$$\mathbf{v} = (\mathbf{v}\cdot\boldsymbol{\nu}_F)\boldsymbol{\nu}_F + \sum_{i=1}^{2}(\mathbf{v}\cdot\boldsymbol{\tau}_{i,F})\boldsymbol{\tau}_{i,F} \quad \text{on } \Gamma_F$$

and the boundary conditions (18) and (19), the integral over the liquid–gas interface becomes

$$\begin{aligned}
-\int_{\Gamma_F}\mathbf{v}\cdot\mathbb{S}(\mathbf{u},p)\cdot\boldsymbol{\nu}_F d\gamma_F &= -\int_{\Gamma_F}\sum_{i=1}^{2}(\mathbf{v}\cdot\boldsymbol{\tau}_{i,F})\boldsymbol{\tau}_{i,F}\cdot\mathbb{S}(\mathbf{u},p) \\
&\quad\cdot\boldsymbol{\nu}_F d\gamma_F - \int_{\Gamma_F}(\mathbf{v}\cdot\boldsymbol{\nu}_F)\boldsymbol{\nu}_F\cdot\mathbb{S}(\mathbf{u},p) \\
&\quad\cdot\boldsymbol{\nu}_F d\gamma_F \\
&= \frac{\mathcal{C}_0}{\mathrm{We}}\int_{\Gamma_F}\sum_{i=1}^{2}(\mathbf{v}\cdot\boldsymbol{\tau}_{i,F})(\boldsymbol{\tau}_{i,F}\cdot\nabla T_F)d\gamma_F \\
&\quad - \frac{1}{\mathrm{We}}\int_{\Gamma_F} M_{T_F}(\mathbf{v}\cdot\boldsymbol{\nu}_F)\mathcal{K}d\gamma_F,
\end{aligned} \tag{33}$$

where $M_{T_F} = (1 - \mathcal{C}_0(T_F - 1))$. The surface tension force given by the second term in (33) contains the temperature dependent surface tension coefficient and the curvature. Hence, the approximations of the temperature and the curvature have to be very accurate in order to avoid unphysical flows in the droplet. One of the popular techniques is based on the replacement of the curvature vector $\mathcal{K}\boldsymbol{\nu}_F$ by the Laplace–Beltrami operator applied to the identity id_{Γ_F} followed by an integration by parts [36,37,48]. The main advantages of this technique are

- the surface tension force can be computed for piecewise smooth surfaces,
- only first derivatives of the basis functions are needed,
- the surface tension force can be treated semi-implicitly giving additional stability,
- the contact angle at the moving contact line can be incorporated directly.

In order to explain this technique in more detail we need some facts from differential geometry. Let $U \subset \mathbb{R}^3$ be an open set with $\Gamma_F \subset U$. For a scalar function f given on U, we define the components of the tangential gradient by

$$(\underline{\nabla} f)_i := \delta_i f = \partial_i f - (\boldsymbol{\nu}_F\cdot\nabla f)\nu_{F,i}, \quad i = 1,2,3.$$

It turns out that the restriction of $\underline{\nabla} f$ onto $\Gamma_F(t)$ depends only on the values of f on $\Gamma_F(t)$. The Laplace–Beltrami operator applied to f is defined as

$$\underline{\Delta} f := \underline{\nabla}\cdot(\underline{\nabla} f) = \sum_{i=1}^{3}\delta_i(\delta_i f). \tag{34}$$

Its application to vector-valued function is understood in a component-wise manner. We replace the curvature vector $\mathcal{K}\nu_F$ in (33) by the Laplace–Beltrami operator applied to the identity $\underline{\Delta} id_{\Gamma_F}$ and integrate by parts [49,50] to get

$$\begin{aligned}
-\frac{1}{\mathrm{We}}\int_{\Gamma_F} M_{T_F}\mathbf{v}\cdot\boldsymbol{\nu}_F\mathcal{K}d\gamma_F &= -\frac{1}{\mathrm{We}}\int_{\Gamma_F} M_{T_F}\underline{\Delta} id_{\Gamma_F}\cdot\mathbf{v}\,d\gamma_F \\
&= \frac{1}{\mathrm{We}}\int_{\Gamma_F}\underline{\nabla} id_{\Gamma_F} \\
&\quad : \underline{\nabla}(M_{T_F}\mathbf{v})\,d\gamma_F - \frac{1}{\mathrm{We}}\int_{\zeta}(\boldsymbol{\nu}_\zeta\cdot\underline{\nabla} id_{\Gamma_F}) \\
&\quad\cdot M_{T_F}\mathbf{v}d\zeta \\
&= \frac{1}{\mathrm{We}}\int_{\Gamma_F}\underline{\nabla} id_{\Gamma_F} \\
&\quad : [M_{T_F}\underline{\nabla}\mathbf{v} + \mathbf{v}\otimes\underline{\nabla} M_{T_F}]\,d\gamma_F - \frac{1}{\mathrm{We}} \\
&\quad\times\int_{\zeta}\boldsymbol{\nu}_\zeta\cdot M_{T_F}\mathbf{v}d\zeta.
\end{aligned} \tag{35}$$

Here, we used $\boldsymbol{\nu}_\zeta\cdot\boldsymbol{\nu}_F = 0$ such that $\boldsymbol{\nu}_\zeta\cdot\underline{\nabla} id_{\Gamma_F} = \boldsymbol{\nu}_\zeta\cdot\nabla id_{\Gamma_F} = \boldsymbol{\nu}_\zeta$. Note, that the last term in (35), which does not appear for closed surfaces Γ_F, is an integral over the contact line ζ and $\boldsymbol{\nu}_\zeta$ is the co-normal vector at the contact line which is normal to ζ and tangent to Γ_F. Let $\boldsymbol{\tau}_S$ be the scaled projection of $\boldsymbol{\nu}_F$ onto the plane Γ_S such that $|\boldsymbol{\tau}_S| = 1$ that means

$$\boldsymbol{\tau}_S := \frac{\boldsymbol{\nu}_F - (\boldsymbol{\nu}_F\cdot\boldsymbol{\nu}_S)\boldsymbol{\nu}_S}{|\boldsymbol{\nu}_F - (\boldsymbol{\nu}_F\cdot\boldsymbol{\nu}_S)\boldsymbol{\nu}_S|}.$$

Then, $\boldsymbol{\nu}_\zeta\cdot\boldsymbol{\tau}_S = \cos(\theta)$ where θ is the contact angle at the moving contact line. In order to incorporate the contact angle into the model, we decompose the test function $\mathbf{v}$ into

$$\mathbf{v} = (\mathbf{v}\cdot\boldsymbol{\nu}_S)\boldsymbol{\nu}_S + (\mathbf{v}\cdot\boldsymbol{\tau}_S)\boldsymbol{\tau}_S + (\mathbf{v}\cdot\boldsymbol{\tau}_S^\perp)\boldsymbol{\tau}_S^\perp,$$

where $\boldsymbol{\tau}_S^\perp$ is a unit vector perpendicular to $\boldsymbol{\nu}_S$ and $\boldsymbol{\tau}_S$. Now, computing the inner product $\boldsymbol{\nu}_\zeta\cdot\mathbf{v}$ in the last term of (35) we use $\mathbf{v}\cdot\boldsymbol{\nu}_S = 0$ on Γ_S for all $\mathbf{v} \in V$ and the orthogonality $\boldsymbol{\nu}_\zeta\cdot\boldsymbol{\tau}_S^\perp = 0$ of the co-normal to get

$$\int_\zeta \boldsymbol{v}_\zeta \cdot M_{T_F}\mathbf{v}\,d\zeta = \int_\zeta (\boldsymbol{v}_\zeta \cdot \boldsymbol{\tau}_S)(\mathbf{v}\cdot\boldsymbol{\tau}_S)M_{T_F}d\zeta = \int_\zeta \cos(\theta)\, M_{T_F}\mathbf{v}\cdot\boldsymbol{\tau}_S d\zeta. \tag{36}$$

Using the derivations (30)–(33), (35) and (36) the weak form of the Navier–Stokes equation reads:

For given $\mathbf{u}(0)$, find $(\mathbf{u},p)\in V\times Q$ such that

$$\left(\frac{\partial \mathbf{u}}{\partial t},\mathbf{v}\right)_{\Omega_F} + a(\mathbf{u};\mathbf{u},\mathbf{v}) - b(p,\mathbf{v}) + b(q,\mathbf{u}) = f(\mathcal{K};\mathbf{v}) \tag{37}$$

for all $(\mathbf{v},q)\in V\times Q$. Here, the forms a, b and f are given by

$$\begin{aligned} a(\hat{\mathbf{u}};\mathbf{u},\mathbf{v}) &= \int_{\Omega_F}\frac{2}{\mathrm{Re}}\mathbb{D}(\mathbf{u}):\mathbb{D}(\mathbf{v}) + (\hat{\mathbf{u}}\cdot\nabla)\mathbf{u}\cdot\mathbf{v}dx \\ &\quad + \frac{1}{\beta_\epsilon}\int_{\Gamma_S}\sum_{i=1}^{2}(\mathbf{u}\cdot\boldsymbol{\tau}_{i,S})(\mathbf{v}\cdot\boldsymbol{\tau}_{i,S})d\gamma_S, \\ b(q,\mathbf{v}) &= \int_{\Omega_F} q\,\nabla\cdot\mathbf{v}dx, \\ f(\mathcal{K};\mathbf{v}) &= \frac{1}{\mathrm{Fr}}\int_{\Omega_F}\mathbf{e}\cdot\mathbf{v}dx + \frac{1}{\mathrm{We}}\int_\zeta \cos(\theta)\, M_{T_F}\mathbf{v}\cdot\boldsymbol{\tau}_S d\zeta \\ &\quad - \frac{1}{\mathrm{We}}\int_{\Gamma_F}\underline{\nabla} id_{\Gamma_F} : [M_{T_F}\underline{\nabla}\mathbf{v} + \mathbf{v}\otimes\underline{\nabla}M_{T_F}]\,d\gamma_F \\ &\quad - \frac{\mathcal{C}_0}{\mathrm{We}}\int_{\Gamma_F}\sum_{i=1}^{2}(\mathbf{v}\cdot\boldsymbol{\tau}_{i,F})(\boldsymbol{\tau}_{i,F}\cdot\nabla T_F)d\gamma_F. \end{aligned}$$

3.2. Weak form of the energy equation

We start with multiplying (20) with a test function $\psi_F\in H^1(\Omega_F)$, integrating by parts, incorporating the boundary condition (24) and using the transition condition (25) to get

$$\begin{aligned} &\int_{\Omega_F}\frac{\partial T_F}{\partial t}\psi_F dx + \int_{\Omega_F}(\mathbf{u}\cdot\nabla)T_F\psi_F\,dx + \frac{1}{\mathrm{Pe}_F}\int_{\Omega_F}\nabla T_F\cdot\nabla\psi_F\,dx \\ &\quad + \int_{\Gamma_F}\frac{\mathrm{Bi}}{\mathrm{Pe}_F}T_F\psi_F d\gamma_F \\ &= -\frac{1}{\mathrm{Pe}_F}\frac{\lambda_S}{\lambda_F}\int_{\Gamma_S}\frac{\partial T_S}{\partial \nu_S}\psi_F d\gamma_F. \end{aligned} \tag{38}$$

Similarly, we multiply (21) with a test function $\psi_S\in H^1(\Omega_S)$, integrate by parts and incorporate the boundary condition (27) to obtain

$$\int_{\Omega_S}\frac{\partial T_S}{\partial t}\psi_S dx + \frac{1}{\mathrm{Pe}_S}\int_{\Omega_S}\nabla T_S\cdot\nabla\psi_S dx = \frac{1}{\mathrm{Pe}_S}\int_{\Gamma_S}\frac{\partial T_S}{\partial \nu_S}\psi_S d\gamma_S. \tag{39}$$

In order to write the energy equations (38) and (39) in a one-field formulation in the domain $\Omega(t) := \Omega_F(t)\cup\Omega_S\cup\Gamma_S(t)$, we define

$$\begin{aligned} \mathbf{u}_T(x,t) &= \begin{cases}\mathbf{u}(x,t) & \text{if}\quad x\in\Omega_F(t),\\ 0 & \text{if}\quad x\in\Omega_S,\end{cases} \\ T(x,t) &= \begin{cases}T_F(x,t) & \text{if}\quad x\in\Omega_F(t),\\ T_S(x,t) & \text{if}\quad x\in\Omega_S,\end{cases} \\ \mathrm{Pe}(x) &= \begin{cases}\mathrm{Pe}_F & \text{if}\quad x\in\Omega_F(t),\\ \frac{\lambda_F}{\lambda_S}\mathrm{Pe}_F & \text{if}\quad x\in\Omega_S,\end{cases} \\ T_0(x) &= \begin{cases}T_{F,0}(x) & \text{if}\quad x\in\Omega_F(t),\\ T_{S,0}(x) & \text{if}\quad x\in\Omega_S.\end{cases} \end{aligned}$$

Moreover, let $g(x)=1$ in $\Omega_F(t)$ and $g(x)=\lambda_S\mathrm{Pe}_S/(\lambda_F\mathrm{Pe}_F)$ in Ω_S. Then, multiplying (39) with $\lambda_S\mathrm{Pe}_S/(\lambda_F\mathrm{Pe}_F)$ and adding to (38) we end up with the weak one-field formulation of the energy equation:

For given $\Omega(0), \mathbf{u}_T$ and T_0, find $T\in H^1(\Omega)$ such that for all $\psi\in H^1(\Omega)$

$$\left(g\frac{\partial T}{\partial t},\psi\right)_\Omega + a_T(\mathbf{u}_T;T,\psi) + b_T(T,\psi) = 0. \tag{40}$$

The forms a_T and b_T are given by

$$\begin{aligned} a_T(\mathbf{u}_T;T,\psi) &= \int_\Omega\frac{1}{\mathrm{Pe}}\nabla T\cdot\nabla\psi dx + \int_\Omega(\mathbf{u}\cdot\nabla)T\psi dx, b_T(T,\psi) \\ &= \mathrm{Bi}\int_{\Gamma_F}\frac{1}{\mathrm{Pe}}T\psi dx. \end{aligned}$$

3.3. Arbitrary Lagrangian Eulerian (ALE) approach

We consider the impinging droplet problem on a micro scale and exclude topological changes in $\Omega_F(t)$. Thus, the Arbitrary Lagrangian–Eulerian (ALE) approach is an appropriate tool to handle the free surface of the droplet. In the ALE approach, the free surface is resolved by the computational mesh. It allows further to suppress spurious velocities in free surface flows [35].

For each t $\in$ (0, I), we define a family of ALE mappings

$$\mathcal{A}_t : \widehat{\Omega}_F \to \Omega_F(t), \quad \mathcal{A}_t(\mathbf{Y}) = \mathbf{X}(\mathbf{Y},t), \quad \mathbf{Y}\in\widehat{\Omega}_F,$$

where $\widehat{\Omega}_F$ is a reference domain of $\Omega_F(t)$. In practical computations, the initial domain or the previous time-step domain is often taken as the reference domain. We assume that the ALE mapping $\mathcal{A}_t$ is an homeomorphism, i.e. continuous with continuous inverse $\mathcal{A}_t^{-1}$. Further, we assume that the mapping

$$t\to\mathbf{X}(\mathbf{Y},t), \quad \mathbf{Y}\in\widehat{\Omega}_F$$

is differentiable almost everywhere in the time interval $(0,I)$. For any scalar function $v\in C^0(\Omega_F(t))$, we define their corresponding function $\hat{v}\in C^0(\widehat{\Omega}_F)$ as follows:

$$\hat{v} := v\circ\mathcal{A}_t, \quad \text{with} \quad \hat{v}(\mathbf{Y},t) = v(\mathcal{A}_t(\mathbf{Y}),t).$$

The time derivative of $v\in C^0(\Omega_F)$ on the reference frame

$$\left.\frac{\partial v}{\partial t}\right|_{\widehat{\Omega}_F} : \Omega_F(t)\times(0,\mathrm{I})\to\mathbb{R}$$

is defined as

$$\left.\frac{\partial v}{\partial t}\right|_{\widehat{\Omega}_F}(\mathbf{X},t) = \frac{\partial \hat{v}}{\partial t}(\mathbf{Y},t), \quad \mathbf{Y} = \mathcal{A}_t^{-1}(\mathbf{X}).$$

We define the domain velocity $\mathbf{w}$ as

$$\mathbf{w}(\mathbf{X},t) = \left.\frac{\partial \mathbf{X}}{\partial t}\right|_{\widehat{\Omega}_F}.$$

Now, applying the chain rule to the time derivative of $v\circ\mathcal{A}_t$ on the reference frame we get

$$\left.\frac{\partial v}{\partial t}\right|_{\widehat{\Omega}_F} = \left.\frac{\partial v}{\partial t}\right|_{\mathbf{x}} + \left.\frac{\partial \mathbf{X}}{\partial t}\right|_{\widehat{\Omega}_F}\cdot\nabla_{\mathbf{x}}v = \left.\frac{\partial v}{\partial t}\right|_{\mathbf{x}} + \mathbf{w}\cdot\nabla_{\mathbf{x}}v. \tag{41}$$

Thus, to rewrite any equation into the non-conservative ALE form, the time derivative has to be replaced with the time derivative on the reference frame and a convective domain velocity term has to be added. Now, using (41) the variational form of the Navier–Stokes equation (37) in the ALE frame reads:

For given $\Omega(0), \mathbf{u}(0)$, find $(\mathbf{u},p,\mathbf{w})\in V\times Q\times V$ such that for all $(\mathbf{v},q)\in V\times Q$

$$\left(\left.\frac{\partial \mathbf{u}}{\partial t}\right|_{\widehat{\Omega}_F},\mathbf{v}\right)_{\Omega_F} + a(\mathbf{u}-\mathbf{w};\mathbf{u},\mathbf{v}) - b(p,\mathbf{v}) + b(q,\mathbf{u}) = f(\mathcal{K};\mathbf{v})$$

Now, to rewrite the energy equation in an ALE forms, we need an extension of the ALE mapping on $\widehat{\Omega}_F$ onto $\widehat{\Omega}$ with the associated domain velocity $\mathbf{w}_T$ where $\mathbf{w}_T|_{\Omega_F} = \mathbf{w}$. Here, $\widehat{\Omega}$ is a reference domain of $\Omega(t)$. The variational form of the energy equation (40) in the ALE frame reads:

For given $\mathbf{u}_T, \mathbf{w}_T, T(0)$, find $T \in H^1(\Omega)$ such that for all $\psi \in H^1(\Omega)$

$$\left(g\frac{\partial T}{\partial t}\Big|_{\widehat{\Omega}}, \psi\right)_\Omega + a_T(\mathbf{u}_T - \mathbf{w}_T; T, \psi) + b_T(T, \psi) = 0.$$

3.4. 3D-axisymmetric formulation

The computational cost can be drastically reduced when we restrict to a 3D-axisymmetric model. There is no need to start again with the partial differential equation in cylindrical coordinates and derive a suitable variational formulation. Instead we generate the 3D-axisymmetric weak form in the 2D-meridian domain directly from the weak form in 3D-Cartesian coordinates. Introducing cylindrical coordinates, the volume, surface and line integrals in 3D are transformed into area integrals, line integrals and a functional in the contact point as described for interface flows in [21]. In this way the space dimension is reduced by one. Note that this approach leads naturally to boundary conditions along the 'artificial rotational axis' which are already partially included in the weak form.

3.5. Discretization in space and time

We use the fractional-step-Θ scheme as time-discretization [51, Section 3.2] which is strongly A-stable and second order accurate on fixed domains. One step in the fractional-step-Θ scheme consists of a clever combination of three Θ schemes with different step sizes and different Θ. In order not to overload the representation, in the following we will denote by (t_n, t_{n+1}) a subinterval in the fractional-step-Θ scheme. We advect the free surface and interface points $\mathbf{X}^n$ on $\Gamma_F(t_n) \cup \Gamma_S(t_n)$ solving

$$\frac{d\mathbf{X}}{dt} = \mathbf{u}(\mathbf{X}, t)$$

with the implicit Euler scheme

$$\mathbf{X}^{n+1} = \mathbf{X}^n + (t_{n+1} - t_n)\mathbf{u}^{n+1},$$

to obtain the new position of the free surface and interface points, respectively. More details on the mesh handling are given in the next two subsections.

Investigations in [52] show that an implicit handling of the curvature term seem to be needed to hope for unconditional stability. Thus, as in [48,53], we use a semi-implicit approximation of the curvature term (first term in (35))

$$\begin{aligned}\frac{1}{\mathrm{We}}\int_{\Gamma_F(t_{n+1})} M_{T_F}\underline{\nabla} id_{\Gamma_F(t_{n+1})} : \underline{\nabla}\mathbf{v}\, d\gamma_F \\ \approx \frac{1}{\mathrm{We}}\int_{\Gamma_F(t_n)} M_{T_F}\left(\underline{\nabla} id_{\Gamma_F(t_n)} + \delta t_n \mathbf{u}^{n+1}\right) \\ : \underline{\nabla}\mathbf{v}\, d\gamma_F,\end{aligned}$$

with the time step $\delta t_n = t_{n+1} - t_n$. Consequently, the curvature term is splitted into an explicit term on the right hand side of the weak formulation (37)

$$-\frac{1}{\mathrm{We}}\int_{\Gamma_F(t_n)} M_{T_F^n}\underline{\nabla} id_{\Gamma_F(t_n)} : \underline{\nabla}\mathbf{v}\, d\gamma_F,$$

where $T_F^n := T_F(t_n)$, and an implicit term on the left hand side

$$\frac{\delta t_n}{\mathrm{We}}\int_{\Gamma_F(t_n)} M_{T_F^n}\underline{\nabla}\mathbf{u}^{n+1} : \underline{\nabla}\mathbf{v}\, d\gamma_F.$$

Note that this term on the left hand side is symmetric and positive semi-definite and – compared with a fully explicit approach – improves the stability of the discrete system.

Since in the ALE approach the computed velocities are used to move the surface and interface points, high accuracy is required. Further, mass should be conserved and spurious velocities – if there are some – should be suppressed. Therefore, we use second–order inf–sup stable finite element approximations avoiding spurious pressure oscillations [54]. Continuous pressure approximations often generate spurious velocities. In order to suppress them discontinuous pressure approximations are a good choice [35]. But to guarantee the inf–sup stability for discontinuous, piecewise linear pressure approximations on arbitrary shape regular families of meshes we have to enrich the space of continuous, piecewise quadratic functions by cubic bubble functions. We denote this pair shortly as $(P_2^+, P_1^{\mathrm{disc}})$ and use it for the approximation of the velocity components and the pressure. The good mass conservation properties are lying on the fact that up to the first integral moments the divergence is elementwise vanishing. The temperature is approximated in Ω by the standard continuous, piecewise quadratic P_2 element.

3.6. Mesh handling at the liquid–solid interface

In the droplet deformation problem, the free surface vertices adjacent to the contact line may reach the solid surface in the next time step during the droplet spreading, see Fig. 2. Further, the vertices on the liquid–solid interface can move in the tangential direction due to the slip with friction boundary condition. This leads to non-matching grid along the liquid–solid interface if the mesh in the solid domain would be fixed. The liquid–solid interface can be handled by either a non-matching or a matching grid. In the non-matching grid, it is enough to find the displacement of the liquid domain and the domain velocity in the solid phase will be

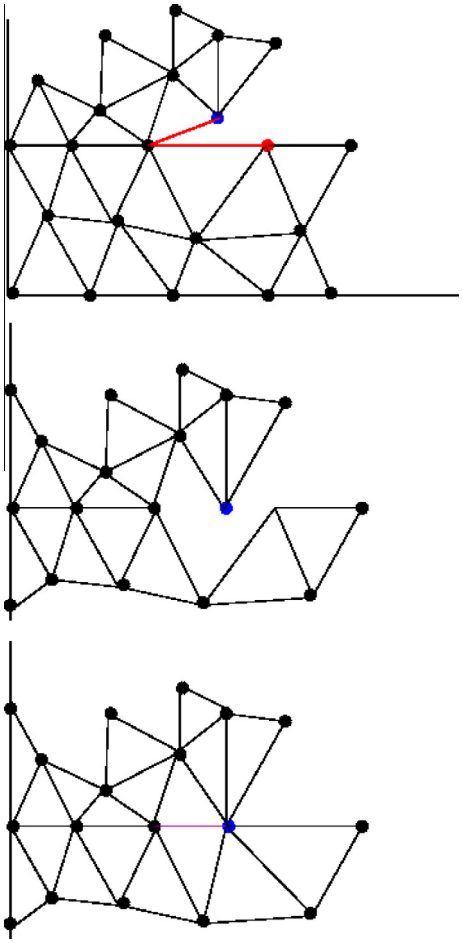

Fig. 2. Mesh adaptive method.

zero. In the matching grid, the displacement of the solid domain also has to be calculated due to the movement of the vertices on the liquid–solid interface. Thus, the domain velocity will be non-zero in solid phase which will induce the domain velocity convection term in the energy equation of the solid phase. In order to handle the non-matching grid at the liquid–solid interface, the mortar finite element method could be used. However, then we would get mortar spaces of time-dependent dimension which are not simple to realize, whereas no special method is needed in the case of a matching grid. That is why we prefer to use matching grids.

Let us explain in more detail the implemented mesh manipulation technique, which maintains a matching grid when a free surface vertex reaches the solid surface. Every time step, after moving the mesh, we calculate the distance between the solid surface and the free surface vertex adjacent to the solid surface. If the distance is less than 10^{-8} or if the free surface vertex is penetrated into the solid surface, we do the following steps to maintain a matching grid before continuing with the next time step:

- Move the free surface vertex perpendicularly to the solid surface and change its type to a contact line (point) vertex. Here, we could move the free surface vertex using the fluid velocity but the vertex is already very close (10^{-8}) to the solid surface and for simplicity we move it perpendicularly to the solid surface, see Fig. 2, top and middle.
- Delete the free surface edge and the solid edge on which the free surface vertex incident, see Fig. 2, middle.
- Reconnect all edges associated with the right side vertex of the solid edge to the moving contact line vertex.
- Generate a new liquid–solid interface edge with the old and new contact line vertex, see Fig. 2, bottom.
- Construct new finite element spaces for the velocity, pressure and temperature on the manipulated mesh.
- Map the nodal values of old finite element functions on the nodal values of the new finite element functions without interpolation.
- Impose the no penetration condition by setting the normal component of the velocity to zero for the degrees of freedom associated with the newly generated liquid–solid interface edge.
- Take the average value from the free surface temperature values and the solid surface temperature values for the temperature degrees of freedom on the newly generated liquid–solid interface edge.

Due to the above mesh manipulation approach, the mesh at the liquid–solid interface remains fitted and thus no mortar (or other) technique is needed. But, due to the tangential movement of the liquid–solid vertices, the displacement of inner points in the solid phase has to be recalculated and this induces a domain velocity convection term in the energy equation of the solid phase. Note, that the mesh manipulation also guarantees a fixed number of cells but only the number of degrees of freedom along the liquid–solid interface and along the free surface may change.

3.7. Linear elastic mesh update

In the elastic mesh update, we calculate the displacement vectors subject to the displacement of the boundary in each time step. The displacement vector Ψ^{n+1} in the domains $\widehat{\Omega}_F(t_n)$ and $\widehat{\Omega}_S$ are obtained by solving linear elasticity equations. For a given boundary displacement Υ^{n+1}, find the displacement Ψ^{n+1} such that

$$\begin{aligned} &\nabla\cdot\mathbb{T}(\Psi^{n+1}) = 0 \quad \text{in } \widehat{\Omega}(t_n)\cup\widehat{\Omega}_S \\ &\Psi^{n+1} = \Upsilon^{n+1} \text{ on } \quad \Gamma_F(t_n)\cup\Gamma_S(t_n)\cup\Gamma_N(t_n) \end{aligned} \tag{42}$$

where

$$\mathbb{T}(\phi) = \lambda_1(\nabla\cdot\phi)\mathbb{I} + 2\lambda_2\mathbb{D}(\phi).$$

Here, λ_1 and λ_2 are Lame constants. To solve problem (42), we use the same triangulation $\mathcal{T}_h$ of the domain which has been taken for the flow and temperature variables and apply a finite element method. The discrete form of Eq. (42) is derived in the usual way:

Find $\Psi_h^{n+1} \in W_h^n := H^1(\widehat{\Omega}(t_n)\cup\widehat{\Omega}_S)$ such that $\Psi_h^n = \Upsilon_h^n$ on $\Gamma_F(t_n)\cup\Gamma_S(t_n)\cup\Gamma_N(t_n)$ and for all $\phi \in W_{h,0}^n$ the relation

$$\int_{\widehat{\Omega}_h(t_n)} \mathbb{D}(\Psi_h^n) : \mathbb{D}(\phi) + C_1 \int_{\widehat{\Omega}_h(t_n)} \nabla\cdot\Psi_h^n \nabla\cdot\phi = 0 \tag{43}$$

holds. Here $C_1 = \lambda_1/\lambda_2$ is a positive constant, which in all our calculations equals 1. The solution of (43) is approximated by continuous, piecewise linear P_1 triangular finite elements since we have to find the displacements of the vertices only and want to have low costs. Also, note that we used the previous time step domain as the reference domain to calculate the mesh velocity. We refer to [55] for a priori bounds and the regularity requirements of mappings in (43).

3.8. Calculating the heat flux across the liquid–solid interface

One of the main objectives of this modeling is to study the heat transfer from the solid phase into the liquid phase during the spreading and recoiling of the droplet for better understanding of the cooling effects. Thus, the crucial parameter in this study is the heat flux across the liquid–solid interface Γ_S from the solid phase into the liquid phase. The heat flux (Q) quantifies the cooling effect in the solid phase, and one of the main objective in spray cooling is to maximize Q. Therefore, the heat flux has to be calculated very accurately. In this section, we present an accurate technique to calculate the heat flux based on the ideas given in [56] for a stationary domain. In the time interval (t^n, t^{n+1}) the heat flux over Γ_S is given by

$$Q := \int_{t^n}^{t^{n+1}} \int_{\Gamma_S} \frac{1}{\mathrm{Pe}_S}\frac{\partial T_S}{\partial \boldsymbol{\nu}_S} d\gamma_S = \int_{t^n}^{t^{n+1}} \int_{\partial\Omega_S} \frac{1}{\mathrm{Pe}_S}\frac{\partial T_S}{\partial \boldsymbol{\nu}_S} d\gamma_S, \tag{44}$$

since $\frac{\partial T_S}{\partial n}\big|_{\partial\Omega_S\setminus\Gamma_S} = 0$, see (11). Let us consider the Dirichlet problem written in ALE frame

$$\begin{aligned} &\frac{\partial T_S}{\partial t}\Big|_{\widehat{\Omega}_S} - \mathbf{w}\cdot\nabla T_S - \nabla\cdot\left(\frac{1}{\mathrm{Pe}_S}\nabla T_S\right) = 0 \quad \text{in } \Omega_S\times(t^n, t^{n+1}), \\ &T_S(X, t^n) = T^n|_{\Omega_S} \quad \text{in } \Omega_S, \\ &T_S = T|_{\partial\Omega_S} \quad \text{on } \partial\Omega_S, \end{aligned} \tag{45}$$

where T_S on $\partial\Omega_S$ is known as the trace of T. Now, multiplying (45) by $v \in H^1(\Omega_S)$ and integrating by parts we get

$$\left(\frac{\partial T_S}{\partial t}\Big|_{\widehat{\Omega}_S} - \mathbf{w}\cdot\nabla T_S, v\right)_{\Omega_S} + \frac{1}{\mathrm{Pe}_S}(\nabla T_S, \nabla v)_{\Omega_S} = \frac{1}{\mathrm{Pe}_S}\int_{\partial\Omega_S}\frac{\partial T_S}{\partial \boldsymbol{\nu}_S} v d\gamma.$$

Since the left hand side is equal to zero for all test functions $v \in H_0^1(\Omega_S)$ (which is just the weak formulation of the Dirichlet problem (45)), the quantity of interest (right hand side for $v = 1$ on $\partial\Omega_S$) is independent of the special choice of

$$v \in \{w \in H^1(\Omega_S) : w = 1 \text{ on } \partial\Omega_S\}.$$

Now integrating over one substep (t^n, t^{n+1}) of the fractional-step-Θ scheme, we get for all $v \in H^1(\Omega_S)$ with $v = 1$ on $\partial\Omega_S$

$$\begin{aligned} Q &:= \frac{1}{\mathrm{Pe}_S}\int_{t^n}^{t^{n+1}} \int_{\partial\Omega_S}\frac{\partial T_S}{\partial \boldsymbol{\nu}_S} d\gamma\, dt \\ &= \left(T_S^{n+1} - T_S^n, v\right)_{\Omega_S} + \int_{t^n}^{t^{n+1}} \left[\frac{1}{\mathrm{Pe}_S}(\nabla T_S, \nabla v)_{\Omega_S} - (\mathbf{w}\cdot\nabla T_S, v)_{\Omega_S}\right] dt. \end{aligned}$$

In the discrete case, we define

$$Q_h := \left(T_{S,h}^{n+1} - T_{S,h}^{n}, v_h\right)_{\Omega_S} + \Theta\,\delta t_n \left[\frac{1}{\mathrm{Pe}_S}\left(\nabla T_{S,h}^{n+1}, \nabla v_h\right)_{\Omega_S} - \left(\mathbf{w}^{n+1}\cdot\nabla T_{S,h}^{n+1}, v_h\right)_{\Omega_S}\right] + (1-\Theta)\,\delta t_n \left[\frac{1}{\mathrm{Pe}_S}\left(\nabla T_{S,h}^{n}, \nabla v_h\right)_{\Omega_S} - \left(\mathbf{w}^{n}\cdot\nabla T_{S,h}^{n}, v_h\right)_{\Omega_S}\right],$$

where Θ is the corresponding value from the substep in the fractional-step-Θ scheme. Note that, as in the continuous case, Q_h is independent from the special choice of the finite element function $v_h \in H^1(\Omega_S)$ with $v_h = 1$ on $\partial\Omega_S$. Let $\varphi_1, \varphi_2, \ldots, \varphi_N$ be the basis function associated with the inner nodes of Ω_S and indices from $N+1$ to $N+M$ be the basis functions associated with the boundary $\partial\Omega_S$ nodes. Then, with v_h as above and

$$T_{S,h} = \sum_{j=1}^{N+M} T_j \varphi_j \quad v_h = \sum_{i=N+1}^{N+M} \varphi_i.$$

Note that $v_h \equiv 1$ at all boundary nodes on $\partial\Omega_S$ and $v_h \equiv 0$ at all inner nodes in Ω_S. Thus, we get

$$Q_h = \sum_{i=N+1}^{N+M}\sum_{j=1}^{N+M}\left\{(T_j^{n+1} - T_j^n)(\varphi_j,\varphi_i)_{\Omega_S} + \Theta\,\delta t_n\, T_j^{n+1}\left[\frac{1}{\mathrm{Pe}_S}(\nabla\varphi_j,\nabla\varphi_i)_{\Omega_S} - (\mathbf{w}^{n+1}\cdot\nabla\varphi_j,\varphi_i)_{\Omega_S}\right] + (1-\Theta)\,\delta t_n\, T_j^n\left[\frac{1}{\mathrm{Pe}_S}(\nabla\varphi_j,\nabla\varphi_i)_{\Omega_S} - \left(\mathbf{w}^{n}\cdot\nabla\varphi_j,\varphi_i\right)_{\Omega_S}\right]\right\}.$$

Therefore, to calculate the heat flux, we need only the mass and the stiffness matrices, but these matrices have been generated already in the assembling process. From the generated matrices $M_{ij} = (\varphi_j,\varphi_i)_{\Omega_S}$ and

$$A_{ij}^{\ell} = \frac{1}{\mathrm{Pe}_S}(\nabla\varphi_j,\nabla\varphi_i)_{\Omega_S} - \left(\mathbf{w}^{\ell}\cdot\nabla\varphi_j,\varphi_i\right)_{\Omega_S} \quad \text{for } \ell \in \{n, n+1\},$$

we compute the vectors

$$m(j) = \left(\varphi_j, \sum_{i=N+1}^{N+M}\varphi_i\right)_{\Omega_S} = \sum_{i=N+1}^{N+M}(\varphi_j,\varphi_i)_{\Omega_S} a^{\ell}(j) = \sum_{i=N+1}^{N+M}\left[\frac{1}{\mathrm{Pe}_S}(\nabla\varphi_j,\nabla\varphi_i)_{\Omega_S} - \left(\mathbf{w}^{\ell}\cdot\nabla\varphi_j,\varphi_i\right)_{\Omega_S}\right].$$

More precisely, we first initialize the vectors $m(j) = 0$ and $a^{\ell}(j) = 0$ for $j = 1,\ldots,N+M$. Then, for each nodal value T_j on $\partial\Omega_S$, that is, for each $T_j, j = N+1,\ldots,N+M$, we identify the j^{th} column in the matrices M and A^{ℓ}. After that we set

$$m(j) = \sum_{i=N+1}^{N+M} M_{i,j}, \quad a^{\ell}(j) = \sum_{i=N+1}^{N+M} A_{i,j}^{\ell}.$$

Note that these vectors have to be calculated before doing any manipulation for imposing boundary conditions. Finally, we compute the heat flux as

$$Q_h = (T^{n+1} - T^n)\cdot m + \Theta\,\delta t_n T^{n+1}\cdot a^{n+1} + (1-\Theta)\,\delta t_n T^n \cdot a^n. \tag{46}$$

Note that the basis functions on the liquid–solid interface have support on both liquid and solid phases. However, to evaluate Q_h we need the contribution only from one side, and we always consider the support of the basis functions from the solid phase in our calculations.

4. Numerical results

In this section, we present an array of numerical results for a 3D-axisymmetric non-isothermal liquid droplet impinging on a horizontal hot solid substrate. Simulations of isothermal impinging droplets have been presented in [21,38,39]. To demonstrate the accuracy of the proposed numerical model, we first compare the simulated results with experimental data given in [57,58], and then the mesh convergence study is performed. After that, we study the influence of the Reynolds number on the flow dynamics of the deforming non-isothermal droplet on a hot substrate. Finally, we run an array of computations to study the thermal effects on the flow dynamics of the droplet by varying the Weber, Peclet, and Biot numbers. Unless specified, we used a constant time step 0.0005, $\beta_\epsilon = 1$ and $C_0 = 0.002$ in all computations. The total number of degrees of freedom of an impinging droplet problem varies during the remeshing, however we have around 14,000 degrees of freedom initially in all test cases with $h = 0.01557859$. Further, a typical simulation of impinging droplet takes approximately nine hours for computing until the dimensionless time $T = 12.5$ using the Intel(R) Core(TM) i7–2600 CPU at 3.40 GHz with 8 GB memory.

4.1. Validation

We first compare the numerically obtained wetting diameter and the apex height of an impinging water droplet with the experimental results given in [57]. We consider a water droplet of diameter $d_0 = 1.29\times10^{-3}$ m impinging on a polished silicon surface with the pre-impact speed of $u_{imp} = 1.18$ m/s, polished test case in Table 1 of [57]. We consider the non-heated case with the equilibrium contact angle $\theta_e = 46°$. Using $L = d_0$ and U = 1.18 m/s as characteristic values, we get $\mathrm{Re} = 1522, \mathrm{We} = 25$ and $\mathrm{Fr} = 110$. Computations are performed with $\beta_\epsilon = 150$, and the initial mesh size is $h = 0.01557859$. The computationally obtained wetting diameter and the apex height of the droplet are compared in Fig. 3 with the experimental results. The droplet attains a maximum dimensionless wetting diameter of 2.1728, and then starts to recoil before attaining the equilibrium state. The wetting diameter fits very well, both qualitatively and quantitatively, with the experimental result even in the recoiling stage. In experiments, an oscillating behavior in the apex height of the droplet has been observed, and it could be due to the capillary waves on the free surface. The numerically obtained apex height curve is more damped, even though the qualitative behavior is similar to experiments. The damping effect has also been observed in the Volume–of–Fluid simulations of 3D–axisymmetric droplets with a dynamic contact angle model, see Fig. 10 in [28]. The axisymmetric assumption in the numerical model could be the reason for this damping effect, and thus a full 3D simulation has to be used in order to capture the surface capillary waves more accurately. To support our argument, we consider another experiment reported in [58] with no capillary waves on the free surface. A water droplet of diameter $d_0 = 2.7\times10^{-3}$ m with $\mathrm{We} = 90$ and $\theta_e = 100°$ is considered. The numerically obtained wetting diameter and the apex height of the droplet are depicted in Fig. 4. The obtained wetting diameter and the apex height are in very good agreement, both qualitatively and quantitatively during the spreading and recoiling stages, with the experimental results reported in Fig. 6 and 7 of [58].

We next perform the mesh convergence study for the proposed numerical scheme. Consider a hemispherical water droplet of diameter $d_0 = 1.29\times10^{-3}$ m with the equilibrium contact angle $\theta_e = 80°$ on a cylindrical substrate. We assume that the droplet is in rest initially. Further, the height and diameter of the solid cylinder are 5×10^{-4} m and 3.8×10^{-2} m respectively. Using $L = d_0$ and U = 1.18 m/s as characteristic values, we get $\mathrm{Re} = 1522, \mathrm{We} = 25$ and $\mathrm{Fr} = 110$. We run an array of simulations with a fixed surface tension by assuming $T_F = T_S = 0$ K to study the mesh convergence of the flow solver. The initial mesh (Level 0) consists of 25 vertices on the free surface with $h = 0.06282152$, and the successive mesh levels are generated by uniformly refining the initial mesh.

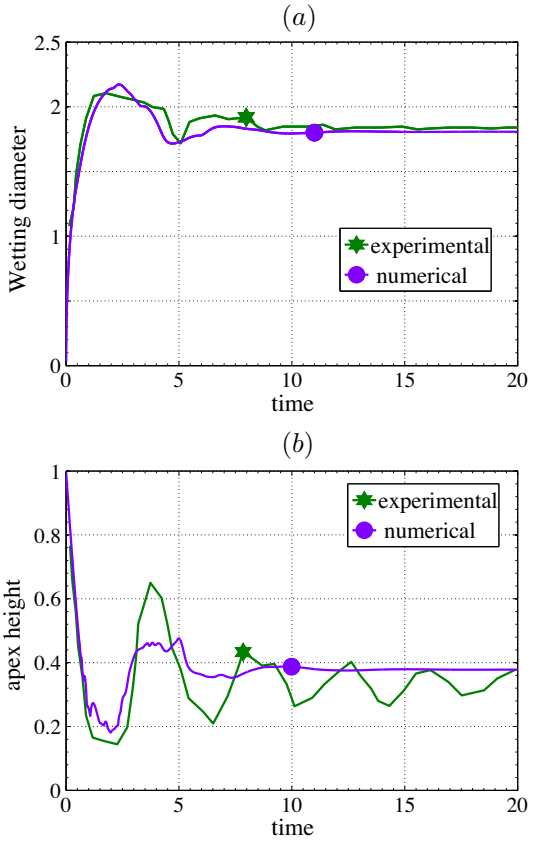

Fig. 3. Comparison with experimental results. (a) wetting diameter, and (b) apex height of a liquid droplet with $\theta_e = 46^\circ$, Re = 1522, We = 25 and Fr = 110.

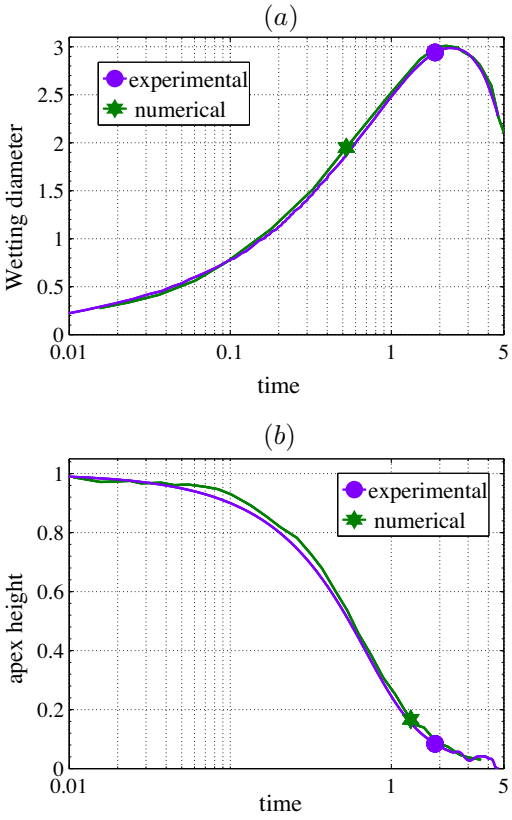

Fig. 4. Comparison with experimental results. (a) wetting diameter, and (b) apex height of a water droplet with $\theta_e = 100^\circ$, We = 90.

All computations are performed with the slip coefficient $\beta_\epsilon = 0.55/h$, where h is the mesh size, and with the time step 0.0005 (Level 0 to 3) and 0.0001 (Level 4), respectively.

Since the initially contact angle (90° due to hemispherical shape) and wetting diameter are not in equilibrium, the droplet slowly starts to oscillate and attains it equilibrium value. The obtained dynamics of the wetting diameter and the dynamic contact angle in all five mesh levels look similar in Fig. 5(a) and (c). A close-up look, however, at the maximal wetting diameter value Fig. 5(b) clearly shows the convergence behavior. A similar mesh convergence behavior has been observed in the dynamic contact angle, see Fig. 5(c) and (d).

We finally perform the mesh convergence study on the heat transfer using the same example with different initial temperature in the solid substrate. In this study we consider the first three mesh levels with the time step 0.0005 and $\beta_\epsilon = 0.55/h$. Further, we used $\mathrm{Pe}_F = \mathrm{Pe}_S = 1$. The obtained heat flux and the total heat flux over time in different mesh levels are presented in Fig. 6. The convergence (in space) of the heat transfer are clearly seen in Fig. 6.

4.2. Influence of the Reynolds number on the flow dynamics

To study the influence of the Reynolds number on the flow dynamics of a non-isothermal water droplet impinging on a hot solid substrate, we consider a droplet of diameter $d_0 = 2.7 \times 10^{-3}$ m. Further, the following material parameters are used: the density ρ = 1000 kg/m^3, the dynamic viscosity μ = 0.001 Ns/m^2, the surface tension σ = 0.073 N/m, the equilibrium contact angle $\theta_e = 30^\circ$. Also, we assume that u_{imp} = 1.54 m/s, $T_{F,0}$ = 298 K, $T_{S,0}$ = 328 K, T_∞ = 298 K, T_{ref} = 323 K (temperature of the fluid surface, the solid surface, the atmospheric and the reference, respectively). Using $L = d_0/2$ and $U = u_{imp}$ as characteristic values, we get $\mathrm{Re} = 2079, \mathrm{We} = 43, \mathrm{Fr} = 179, \mathrm{Pe}_F = 10, \mathrm{Pe}_S = 100, \mathrm{Bi} = 0.000058$ for the considered material parameters. In order to study the influence of the Reynolds number, we considered four variants: (i) Re = 260, (ii) Re = 520, (iii) Re = 1040 and (iv) Re = 2079 by varying the viscosity μ.

We first present the contours of the pressure, velocity, vorticity, and the temperature distribution for the high Reynolds number case Var (iv). Fig. 7 depicts the pressure contours in the droplet of Var (iv) at different instances (dimensionless time) $t = 0.1, 1.0, 2.0, 8.0, 16, 25$. Initially, the pressure variation is large near the contact line. However, the distribution of pressure becomes almost uniform toward the end of simulation. Next, the contour lines of the magnitude of the velocity for the same variant are depicted in Fig. 8. The arrows in each picture represent the flow direction. The vorticity contours in the 3D-axisymmetric impinging droplet during the sequence of spreading and recoiling are depicted in Fig. 9. The observed range of vorticity is high in the high Reynolds number variant in comparison with the low Reynolds number Var (i).

Next, the computationally obtained sequence of droplets in Var (i) and Var (iv) at different instances (dimensionless time) $t = 1.0, 8.0, 16, 25$, are depicted in Figs. 10 and 11 with the solid substrate. The colors in the pictures represent the temperature distribution during the droplet deformation over time. Initially, the dimensionless temperature in the droplet is zero, whereas the temperature in the solid is 1.2143. In the high Reynolds number case, Var (iv), the wetting diameter of the droplet is larger, and thus the droplet covers more solid substrate and absorb more heat from the solid substrate. The total heat flux from the solid phase into the liquid phase will be studies in the Sections 4.4 and 4.5.

Next, the obtained wetting diameter and the dynamic contact angle in all four variants over time are presented in Fig. 12. As expected, the wetting diameter increases when the Reynolds number increase. The maximum wetting diameter and the time

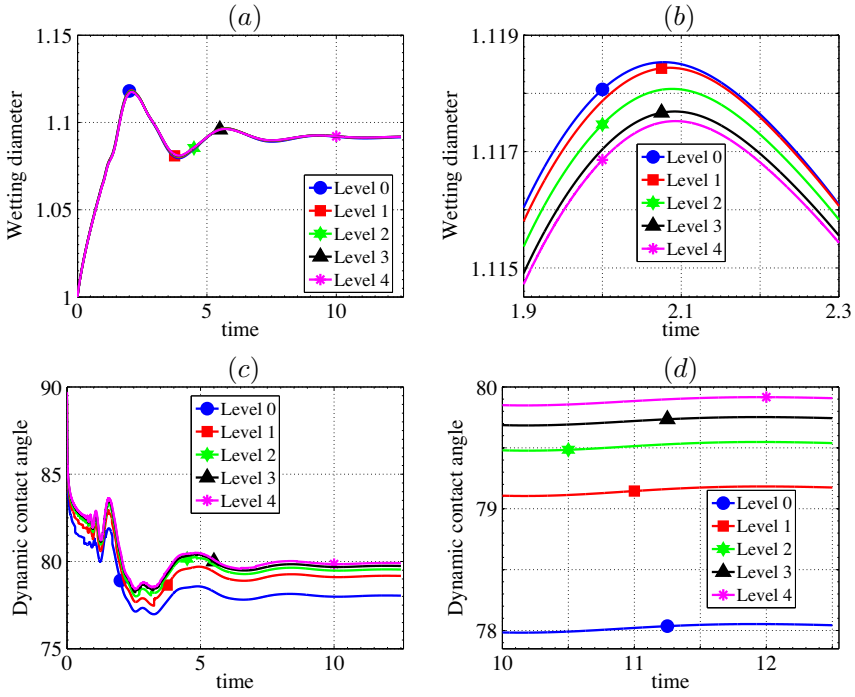

Fig. 5. Mesh convergence study on the flow dynamics of the hemispherical water droplet with Re = 1522, We = 25 and Fr = 110 and θ_e = 80°. The obtained dynamics of the wetting diameter (a) and their close-up at the maximal value (b), the dynamics contact angle (c) and their close-up at the end of the equilibrium stage in five mesh levels.

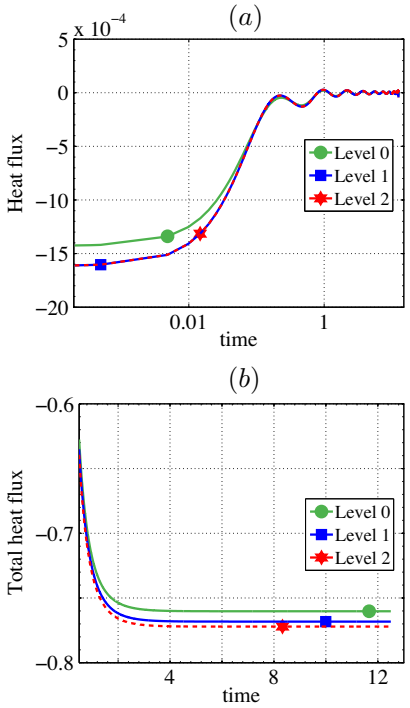

Fig. 6. Mesh convergence study on the heat transfer in the hemispherical water droplet with Re = 1522, We = 25 and Fr = 110 and $\theta_e = 80^\circ$. The obtained heat flux (a) and the total heat flux (b) over time in different mesh levels.

taken to obtain it are presented in Fig. 13. We can observe that the maximum wetting diameter is nonlinear with respect to the Reynolds number, see Fig. 13. A similar behavior is observed in the time taken to attain the maximum wetting diameter. The dynamic contact angle in all four variants reach the equilibrium value almost after the dimensionless time t = 10, see Fig. 12. Further, the maximum relative mass loss in the liquid droplet occurs in Var (iv), and it is 0.42% which shows the accuracy of the numerical scheme.

Remark 1. Since the contact point and the free surface points move with the discrete fluid velocity, a small change in the relative velocity between the contact point and the free surface point next to it will induce wiggles in the dynamics contact angle calculations. Note that the free surface point of the droplet may reach the solid substrate (rolling motion) during spreading. These are the reasons for the wiggles in the curves of Fig. 12. Also, note that in our calculations, the angle between the solid substrate and the first free surface point is calculated as the dynamic contact angle at every time-step.

4.3. Influence of the Weber number on the flow dynamics

To study the influence of the surface tension on the flow dynamics, we vary the Weber number and fix the other dimensionless numbers. We consider the following four variants: (i) We = 43, (ii) We = 90, (iii) We = 140, and (iv) We = 190 by varying the surface tension. Further, we used the fixed numbers Re = 2079, Fr = 179, $Pe_F = 10, Pe_S = 100$, and Bi = 0.000058 in all variants. Also, we set the equilibrium contact angle $\theta_e = 30^\circ$, $T_{F,0} = 298$ K, $T_{S,0} = 328$ K, T_∞ = 298 K, T_{ref} = 323 K.

The computationally obtained wetting diameter and dynamic contact angle over time for all four variants are presented in Fig. 14. Since the surface tension will be large in the Var (i), the maximum wetting diameter is small. As expected, the maximum wetting diameter increases when the Weber number increase. The dynamic contact angle in all four variants reach the equilibrium value almost after the dimensionless time t = 1. However, more oscillations have been observed in Var (iv). Since the surface tension coefficient is very small (less rigid) in this variant, more rolling motion is observed while spreading. Next, the maximum wetting diameter and the time taken to obtain it are presented in Fig. 15. As in the Reynolds number case, the maximum wetting diameter is nonlinear with respect to the Weber number, see

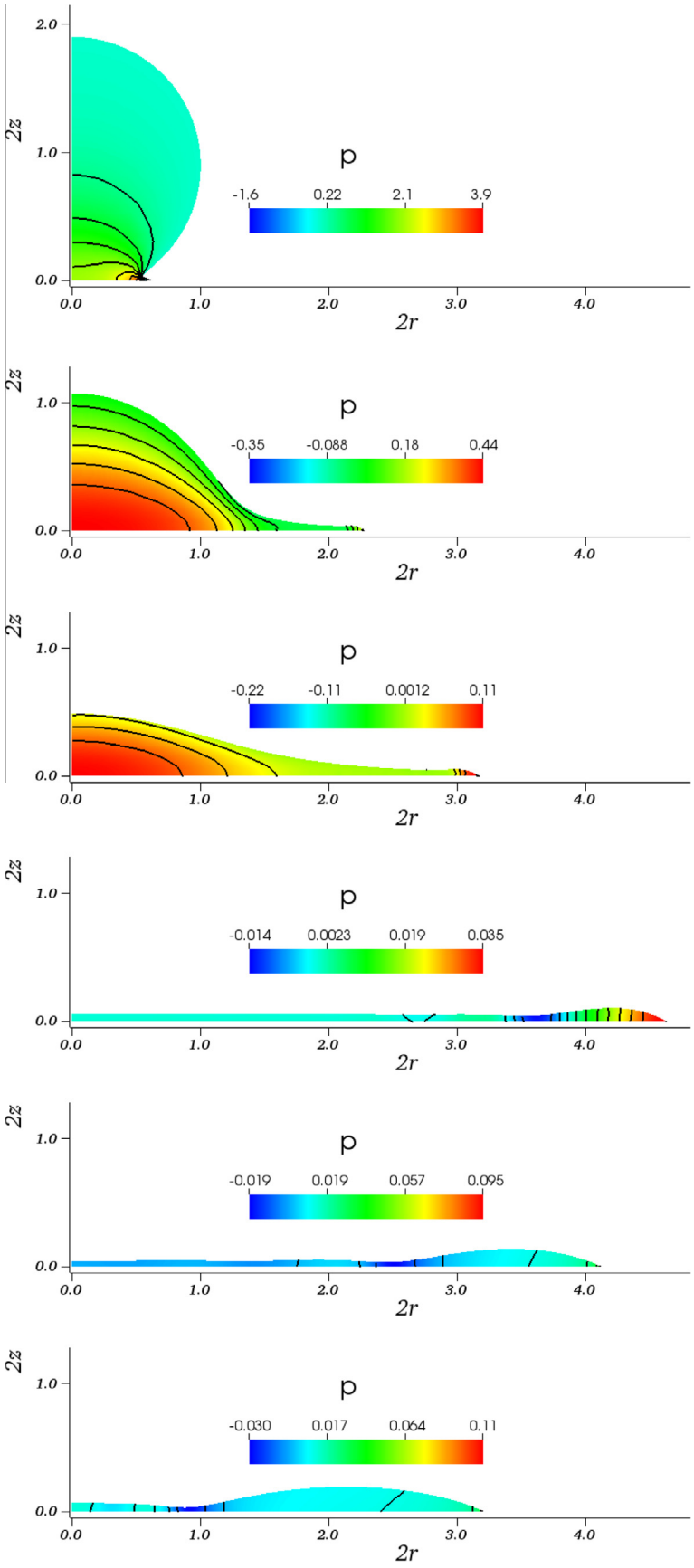

Fig. 7. Pressure contours in the impinging droplet with $\theta_e = 30^\circ$, We = 43, Fr = 179 during spreading and recoiling. Var (iv) Re = 2079. The dimensionless timing from the top: $t = 0.1, 1.0, 2.0, 8.0, 16, 25$.

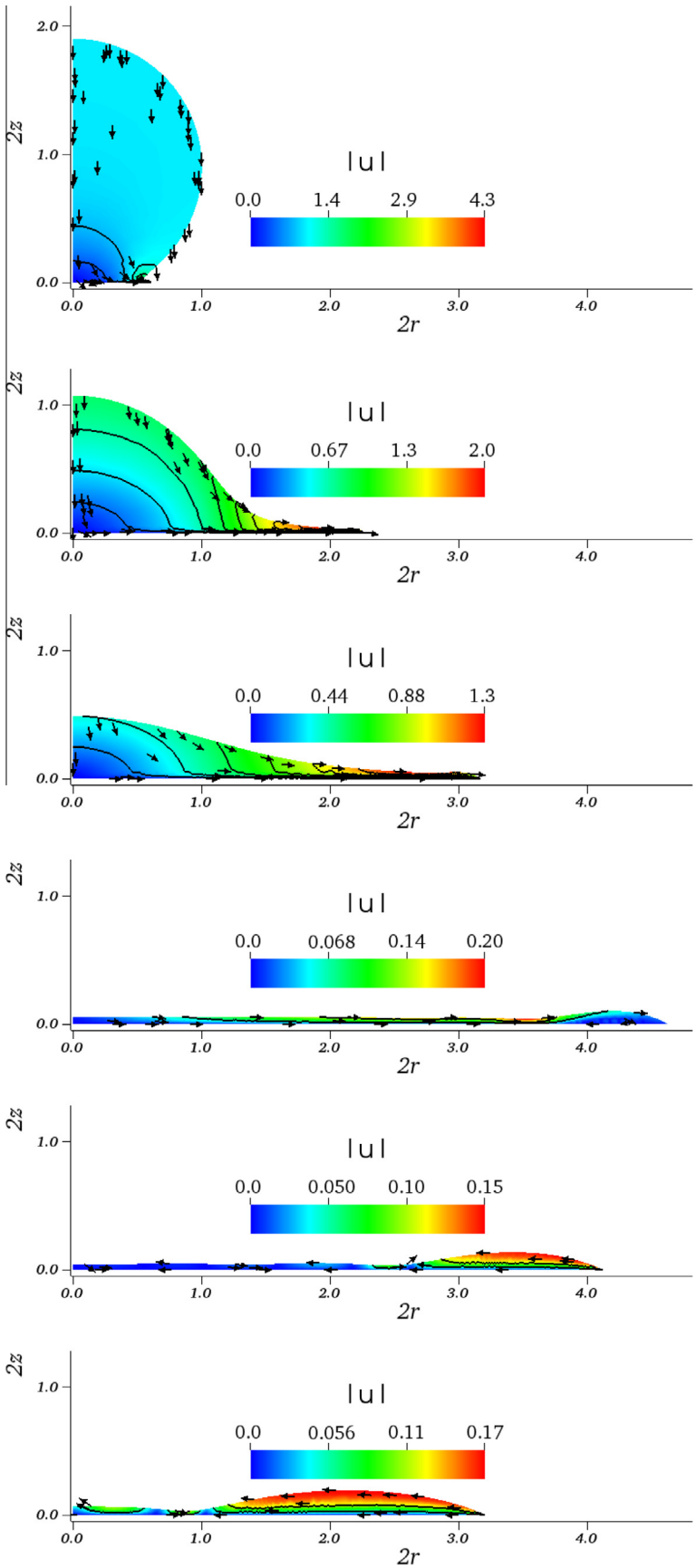

Fig. 8. Velocity (magnitude) contours in the impinging droplet with $\theta_e = 30^\circ$, We $= 43$, Fr $= 179$ during spreading and recoiling. Var (iv) Re = 2079. The dimensionless timing from the top: $t = 0.1, 1.0, 2.0, 8.0, 16, 25$.

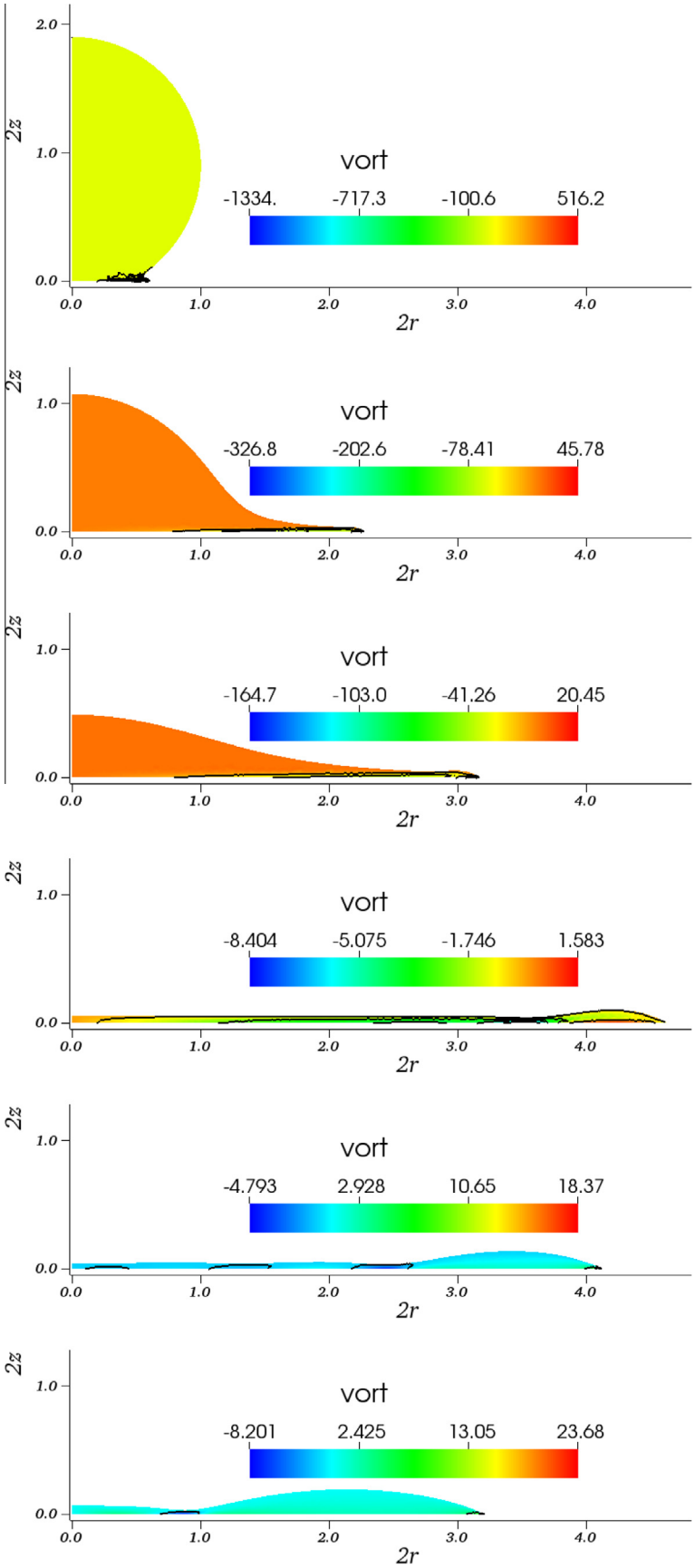

Fig. 9. Vorticity contours in the impinging droplet with $\theta_e = 30^\circ$, We $= 43$, Fr $= 179$ during spreading and recoiling. Var (iv) Re=2079. The dimensionless timing from the top: $t = 0.1, 1.0, 2.0, 8.0, 16, 25$.

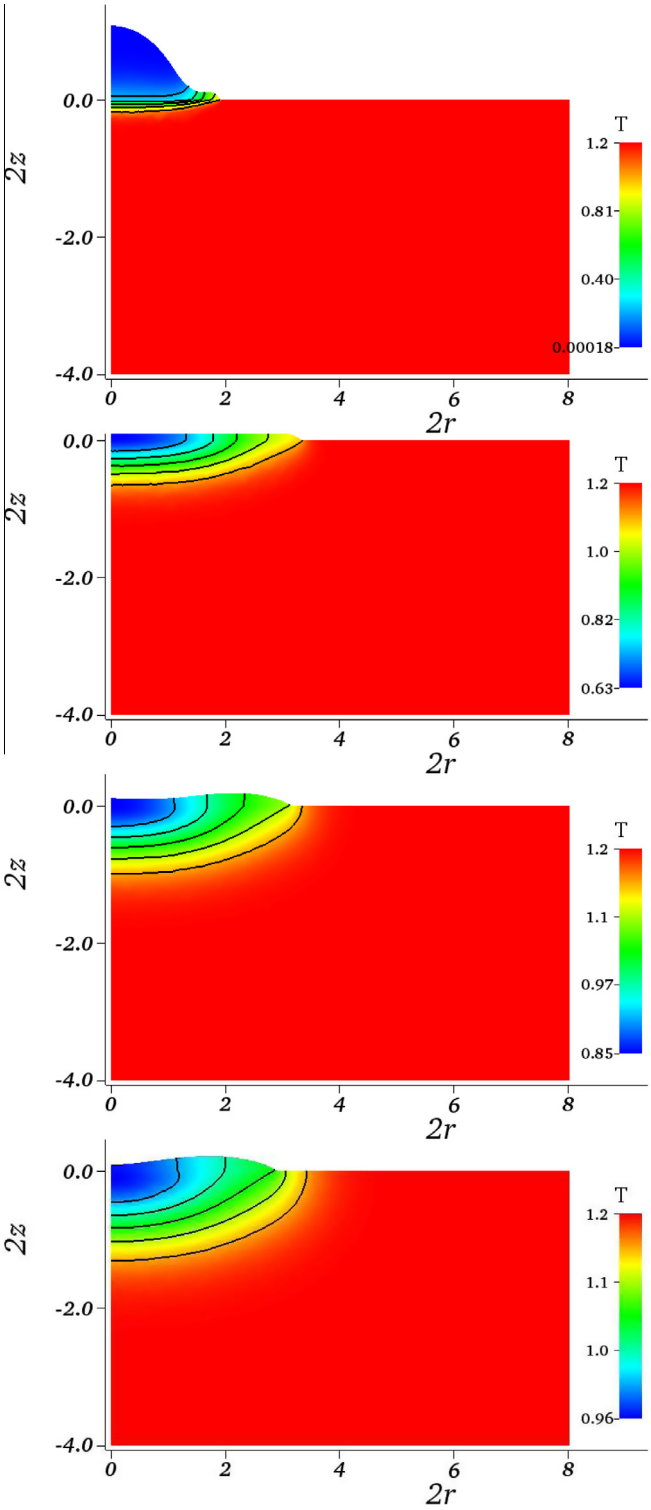

Fig. 10. Sequence of images of a liquid droplet impinging on a hot solid substrate with $\theta_e = 30^\circ$, We = 43, Fr = 179. Var (i) Re = 260. The dimensionless timing from the top: $t = 1.0, 8.0, 16, 25$.

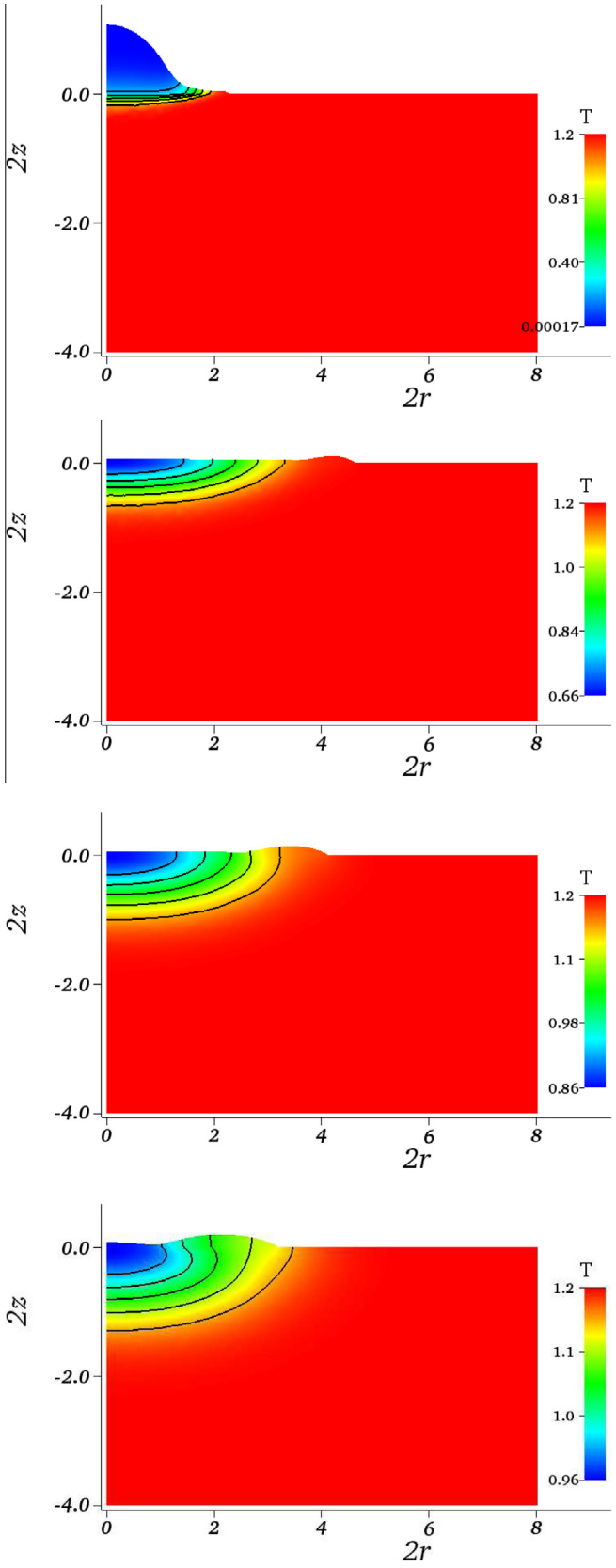

Fig. 11. Sequence of images of a liquid droplet impinging on a hot solid substrate with $\theta_e = 30^\circ$, We = 43, Fr = 179. Var (iv) Re = 2079. The dimensionless timing from the top: $t = 1.0, 8.0, 16, 25$.

Fig. 15. Further, the maximum relative mass loss in the liquid droplet is 0.4% and it occurred in Var (iv).

4.4. Influence of the solid Peclet number on the flow dynamics

In this section we study the influence of the solid Peclet number on the heat transfer. We consider five variants (i) $Pe_S = 50$, (ii) $Pe_S = 100$, (iii) $Pe_S = 250$, (iv) $Pe_S = 350$ and (v) $Pe_S = 400$ by varying the heat conductivity of the solid. Further, we use fixed dimensionless numbers $Re = 2079, Fr = 179, We = 43, Bi = 0.000058, Pe_F = 10$.

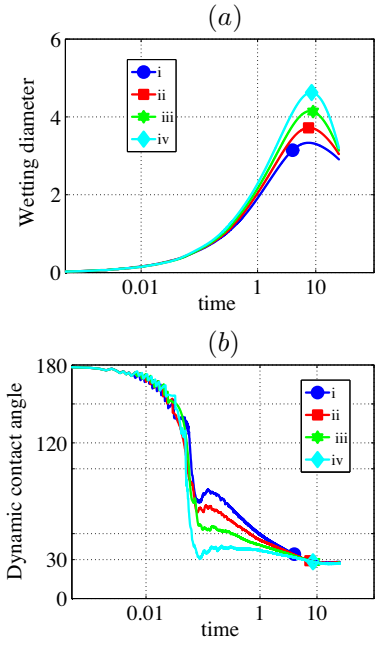

Fig. 12. Wetting diameter (a) and the dynamic contact angle (b) of a liquid droplet with $\theta_e = 30^\circ$, We = 43 and Fr = 179, impinging on a hot solid substrate. (i) Re = 260, (ii) Re = 520, (iii) Re = 1040, (iv) Re = 2079.

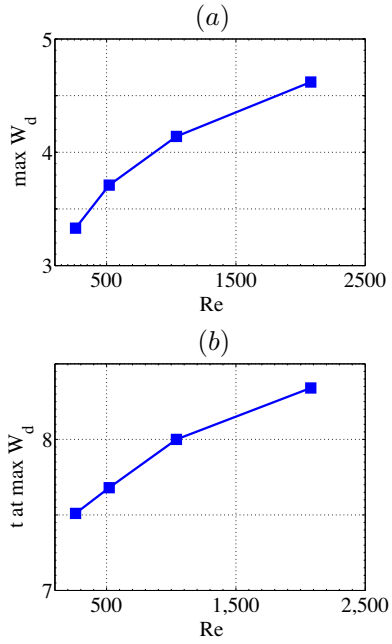

Fig. 13. Maximal wetting diameter (a) and the time to attain it (b) for different Reynolds numbers with fixed We = 43 for a liquid droplet.

The fluid flow indirectly depends on the temperature thorough the surface tension. A change in the local surface temperature T on the free surface induce Marangoni convection. However, in all variants the surface temperature variation is not high. Thus, the flow dynamics is same in all five variants of the solid Peclet number, see the wetting diameter and the dynamic contact angle over time in Fig. 16.

Next, we use the new method in Section 3.8 for calculating the heat flux (Q_h) and the total heat flux (sum over all time intervals) across the liquid–solid interface. The results for all five variants are presented in Fig. 17. Though, the wetting area is same in all variants, the heat flux varies. The heat flux is larger in the small solid

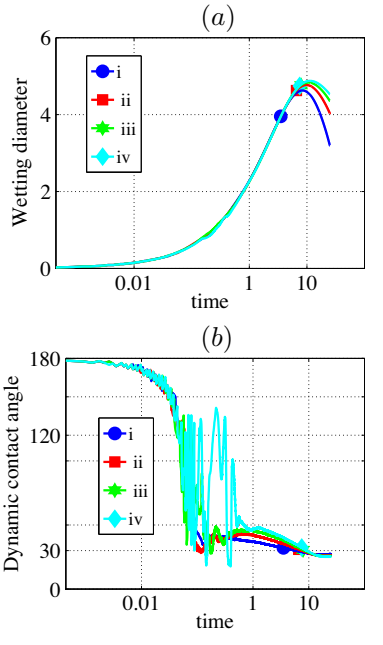

Fig. 14. Wetting diameter (a) and the dynamic contact angle (b) of a liquid droplet with $\theta_e = 30^\circ$, Re = 2079 and Fr = 179, impinging on a hot solid substrate. (i) We = 43, (ii) We = 90, (iii) We = 140 and (iv) We = 190.

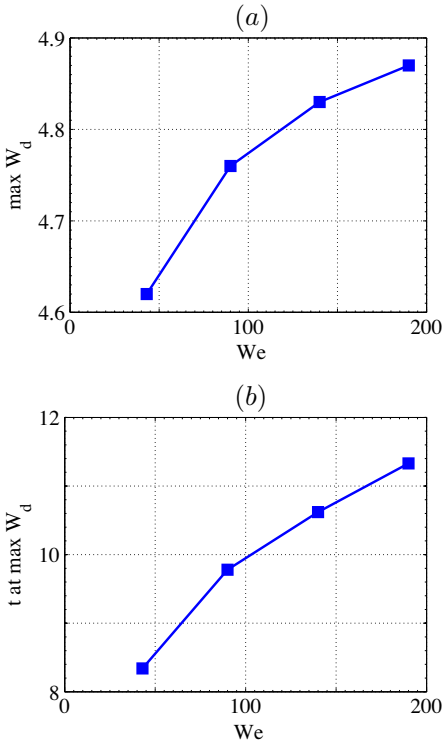

Fig. 15. Maximal wetting diameter (a) and the time to attain it (b) for different Weber numbers with fixed Re = 2079, Fr = 179 and B = 0.000058.

Peclet number Var (i), whereas the heat flux is smaller in the large solid Peclet number Var (v). It is interesting to note that the heat flux is same in all five variants when the wetting diameter is large, say around the dimensionless time $t = 9$, see Fig. 17. During the recoiling, we can see the reverse effect, that is, the heat flux is less in the small solid Peclet number case Var (i), and it approaches zero faster than the other variants. This behavior can clearly be seen in the total heat flux, Fig. 17 (bottom), where there is almost no

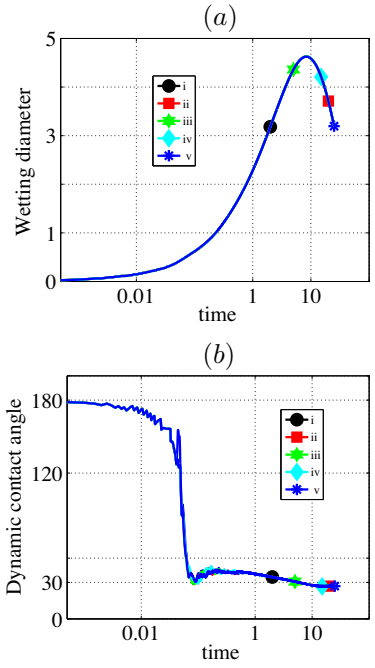

Fig. 16. Wetting diameter (a) and dynamic contact angle (b) of a liquid droplet with $\theta_e = 30^\circ, \mathrm{Re} = 2079, \mathrm{We} = 43$ and Fr = 179, impinging on a hot solid substrate. Variants of solid Peclet number (i) Pe_S = 50, (ii) Pe_S = 100, (iii) Pe_S = 250, (iv) Pe_S = 350 and (v) Pe_S = 400.

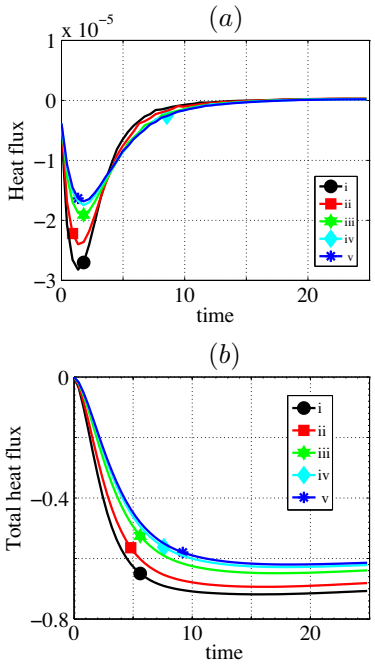

Fig. 17. Heat flux (a) and total heat flux (b) over a liquid–solid interface with $\theta_e = 30^\circ, \mathrm{Re} = 2079, \mathrm{We} = 43$ and Fr = 179, impinging on a hot solid substrate. Variants of solid Peclet number (i) Pe_S = 50, (ii) Pe_S = 100, (iii) Pe_S = 250, (iv) Pe_S = 350 and (v) Pe_S = 400.

variation in the total heat flux of Var (i) after the dimensionless time t = 10.

4.5. Influence of the Biot number on the flow dynamics

In this section we study the influence of the Biot number on the heat flux. We consider a droplet of diameter $d_0 = 3.0 \times 10^{-3}$ m. Further, the following material parameters are used: the density

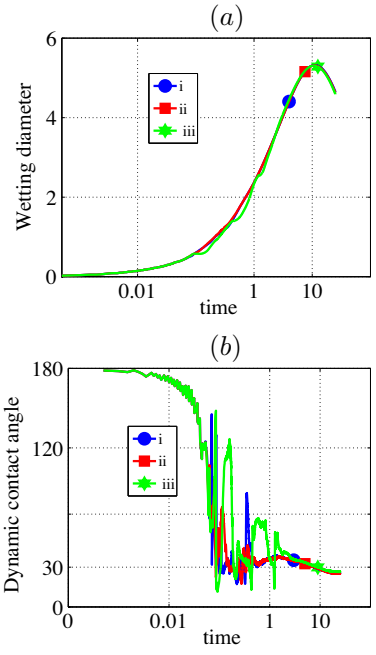

Fig. 18. Wetting diameter (a) and dynamic contact angle (b) of a liquid droplet with $\theta_e = 30^\circ, \mathrm{Re} = 3750, \mathrm{We} = 128, \mathrm{Fr} = 425$, impinging on a hot solid substrate. Variants of Biot number (i) Bi = 0.001, (ii) Bi = 0.1, (iii) Bi = 1.

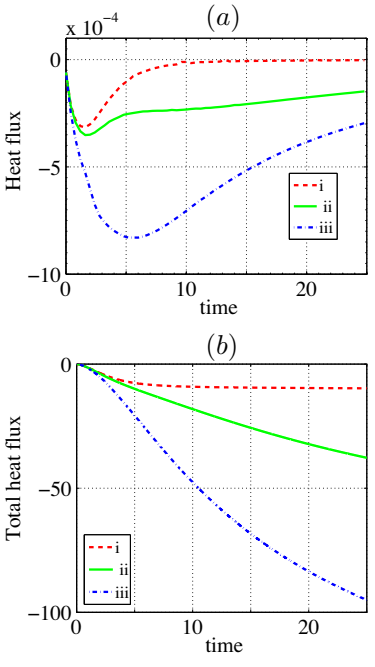

Fig. 19. Influence of the Biot number on the heat flux (a) and on the total heat flux (b) with Re = 3750, We = 128, Fr = 425 (i) Bi = 0.001, (ii) Bi = 0.1, (iii) Bi = 1.

ρ = 1000 kg/m^3, the dynamic viscosity μ = 0.001 Ns/m^2, the surface tension σ = 0.073 N/m, the equilibrium contact angle θ_e = 30°. Also, we assume that $u_{imp} = 2.5$ m/s, $T_{F,0}$=300 K, $T_{S,0}$ = 700 K, T_∞ = 298 K, T_{ref} = 323 K (temperature of the fluid surface, the solid surface, the atmospheric and the reference, respectively). Using $L = d_0/2$ and $U = u_{imp}$ as characteristic values, we get $\mathrm{Re} = 3750, \mathrm{Fr} = 425$, $We = 128, \mathrm{Pe}_F = 10, \mathrm{Pe}_S = 100$. In this study, we consider three variants: (i) Bi = 0.001, (ii) Bi = 0.1 and (iii) Bi = 1. The obtained wetting diameter and the dynamic contact angle over time for all

three variants are presented in Fig. 18. Though the flow dynamics is similar in first two variants, there are some oscillations in the dynamic contact angle of Var (iii). Recall that the Biot number controls the heat flux across the free surface, that is, a large value of Biot number induces more heat flux. Since we use the same liquid Peclet number in all three variants, the temperature on the free surface will be less in case of a large Biot number, Var (iii), in comparison with the Var (i). Therefore, the surface tension force will be larger in Var (iii), see the relation (18), and it induces more rolling motion while spreading.

Next, the obtained heat flux and the total heat flux across the liquid–solid interface over time are presented in Fig. 19. As expected, the heat flux is large in the high Biot number case Var (iii). The heat flux in Var (i) approaches zero when the droplet attains it maximum wetting diameter, whereas the heat transfer from the solid phase to the liquid phase occurs even during the recoiling stage in the Var (iii), see Fig. 19.

5. Summary

A finite element scheme using the arbitrary Lagrangian–Eulerian (ALE) approach for computations of a non-isothermal liquid droplet impinging on a horizontal hot solid substrate is presented in this paper. The coupled Navier–Stokes and the energy equations are solved using this numerical scheme. The derivation of the energy equations in solid and liquid phases into a single variational equation makes the scheme robust in the ALE approach. The highlights of the numerical scheme are the Laplace–Beltrami operator technique for the curvature approximation and the contact angle inclusion, the ALE approach with moving meshes in both the liquid and the solid phase to track the free surface and to guarantee matching grids at the liquid–solid interface, and the special algorithm for calculating the heat flux without differentiating the numerical solution. The proposed numerical scheme works well without loss of accuracy even for problems with large jumps in the material parameters across the liquid–solid interface. An array of numerical experiments by varying the Reynolds, Weber, Peclet, and Biot numbers are performed for a 3D–axisymmetric non-isothermal liquid droplet impinging on a horizontal hot solid substrate.

Conflict of interest

None declared.

Acknowledgement

The authors would like to thank the German research foundation (DFG, GRK 1554) and the National Board for Higher Mathematics (NBHM), India for partially supporting this research.

References

[1] C. Hirt, B. Nichols, Volume of Fluid (VOF) method for the dynamics of free boundaries, J. Comput. Phys. 39 (1981) 201–225.
[2] J.E. Pilliod, E.G. Puckett, Second-order accuarate volume-of-fluid algorithms for tracking material interfaces, J. Comput. Phys. 199 (2) (2004) 465–502.
[3] M. Renardy, Y. Renardy, J. Li, Numerical simulation of moving contact line problems using a volume-of-fluid method, J. Comput. Phys. 171 (2001) 243–263.
[4] W. Rider, D. Kothe, Reconstructing volume tracking, J. Comput. Phys. 141 (1998) 112–152.
[5] M. van Sint Annaland, N. Deen, J. Kuipers, Numerical simulation of gas bubbles behaviour using a three-dimensional volume of fluid method, Chem. Eng. Sci. 60 (11) (2005) 2999–3011.
[6] S. Osher, J.A. Sethian, Fronts propagating with curvature dependent speed: algorithms based on Hamilton–Jacobi forumlations, J. Comput. Phys. 79 (1988) 12–49.
[7] M. Sussman, P. Smereka, S. Osher, A level set approach for computing solutions to incompressible two-phase flow, J. Comput. Phys. 114 (1) (1994) 146–159.
[8] J.A. Sethian, Level Set Methods, Cambridge University Press, 1996.
[9] M. Sussman, E.G. Puckett, A coupled level set and volume-of-fluid method for computing 3d axisymmetric incompressible two-phase flows, J. Comput. Phys. 162 (2000) 301–337.
[10] S. Gross, V. Reichelt, A. Reusken, A finite element based level set method for two-phase incompressible flows, Comput. Visual. Sci. 9 (4) (2006) 239–257.
[11] C.S. Peskin, Flow patterns around heart valves: a numerical method, J. Comput. Phys. 10 (1972) 252–271.
[12] S. Unverdi, G. Tryggvason, A front-tracking method for viscous, incompressible multi-fluid flows, J. Comput. Phys. 100 (1992) 25–37.
[13] K.S. Sheth, C. Pozrikidis, Effects of inertia on the deformation of liquid drops in simple shear flow, Comput. Fluids 24 (2) (1995) 101–119.
[14] G. Tryggvason, B. Bunner, A. Esmaeeli, D. Juric, N. Al-Rawahi, W. Tauber, J. Han, S. Nas, Y.-J. Jan, A front-tracking method for the computations of multiphase flow, J. Comput. Phys. 169 (2) (2001) 708–759.
[15] C.S. Peskin, The immersed boundary method, Acta Numer. (2002) 1–36.
[16] C.W. Hirt, A.A. Amsden, J.L. Cook, An arbitrary Lagrangian Eulerian computing method for all flow speeds, J. Comput. Phys. 14 (3) (1974) 227–253.
[17] J. Donéa, Arbitrary Lagrangian–Eulerian finite element methods, in: T. Belytschko, T.R.J. Hughes (Eds.), Computational Methods for Transient Analysis, Elsevier scientific publishing co, Amsterdam, 1983, pp. 473–516.
[18] F. Nobile, Numerical approximation of fluid-structure interaction problems with application to haemodynamics (Ph.D. thesis), École Polytechnique Fédérale de Lausanne, 2001.
[19] P. Nithiarasu, An arbitrary Lagrangian Eulerian (ALE) formulation for free surface flows using the characteristic-based split (CBS) scheme, Int. J. Numer. Methods Fluids 12 (2005) 1415–1428.
[20] S. Ganesan, L. Tobiska, Computations of flows with interfaces using arbitrary Lagrangian Eulerian method, in: Proceedings of ECCOMAS CFD 2006, Egmond aan Zee, The Netherlands, ISBN 90-9020970-0.
[21] S. Ganesan, L. Tobiska, An accurate finite element scheme with moving meshes for computing 3D-axisymmetric interface flows, Int. J. Numer. Methods Fluids 57 (2) (2008) 119–138.
[22] H. Fujimoto, N. Hatta, Deformation and rebounding processes of a water droplet impinging on a flat surface above leidenfrost temperature, J. Fluids Eng. 118 (1996) 142–149.
[23] M. Pasandideh-Fard, R. Bhola, S. Chandra, J. Mostaghimi, Deposition of tin droplets on a steel plate: simulations and experiments, Int. J. Heat Mass Transfer 41 (1998) 2929–2945.
[24] D.J.E. Harvie, D.F. Fletcher, A hydrodynamic and thermodynamic simulation of droplet impacts on hot surfaces. Part II: validation and applications, Int. J. Heat Mass Transfer 44 (14) (2001) 2643–2659.
[25] R. Ghafouri-Azar, S. Shakeri, S. Chandra, J. Mostaghimi, Interactions between molten metal droplets impinging on a solid surface, Int. J. Heat Mass Transfer 46 (8) (2003) 1395–1407.
[26] G. Strotos, M. Gavaises, A. Theodorakakos, G. Bergeles, Numerical investigation on the evaporation of droplets depositing on heated surfaces at low weber numbers, Int. J. Heat Mass Transfer 51 (7–8) (2008) 1516–1529.
[27] G. Strotos, M. Gavaises, A. Theodorakakos, G. Bergeles, Numerical investigation of the cooling effectiveness of a droplet impinging on a heated surface, Int. J. Heat Mass Transfer 51 (19–20) (2008) 4728–4742.
[28] A.M. Briones, J.S. Ervin, S.A. Putnam, L.W. Byrd, L. Gschwender, Micrometer-sized water droplet impingement dynamics and evaporation on a flat dry surface, Langmuir 26 (16) (2010) 13272–13286.
[29] S.A. Putnam, A.M. Briones, L.W. Byrd, J.S. Ervin, M.S. Hanchak, A. White, J.G. Jones, Microdroplet evaporation on superheated surfaces, Int. J. Heat Mass Transfer 55 (21–22) (2012) 5793–5807.
[30] L.S.F.Y. Ge, Three-dimensional simulation of impingement of a liquid droplet on a flat surface in the leidenfrost regime, Phys. Fluids 17 (2005) 027104.
[31] L.S.F.Y. Ge, 3-D modeling of the dynamics and heat transfer characteristics of subcooled droplet impact on a surface with film boiling, Int. J. Heat Mass Transfer 49 (21–22) (2006) 4231–4249.
[32] M. Francois, W. Shyy, Computations of drop dynamics with the immersed boundary method, Part 1: Numerical algorithm and buoyancy-induced effect, Numer. Heat Transfer, Part B: Fundam. 44 (2) (2003) 101–118.
[33] M. Francois, W. Shyy, Computations of drop dynamics with the immersed boundary method, Part 2: Drop impact and heat transfer, Numer. Heat Transfer, Part B: Fundam. 44 (2) (2003) 119–143.
[34] J.F.Z. Zhao, D. Poulikakos, Heat transfer and fluid dynamics during the collision of a liquid droplet on a substrate. 1. Modeling, Int. J. Heat Mass Transfer 39 (13) (1996) 2771–2789.
[35] S. Ganesan, G. Matthies, L. Tobiska, On spurious velocities in incompressible flow problems with interfaces, Comput. Methods Appl. Mech. Eng. 196 (7) (2007) 1193–1202.
[36] G. Dziuk, Finite elements for the Beltrami operator on arbitrary surfaces, in: S. Hildebrandt, R. Leis (Eds.), Partial Differential Equations and Calculus of Variations, Springer, Berlin, 1988, pp. 142–155.
[37] G. Dziuk, An algorithm for evolutionary surfaces, Numer. Math. 58 (1991) 603–611.
[38] S. Ganesan, Finite element methods on moving meshes for free surface and interface flows (Ph.D. thesis), Otto-von-Guericke-Universitaẗ, Fakultät fuï Mathematik, Magdeburg, 2006.
[39] S. Ganesan, L. Tobiska, Modelling and simulation of moving contact line problems with wetting effects, Comput. Visual. Sci. 12 (2009) 329–336.

[40] M. Behr, F. Abraham, Free-surface flow simulations in the presence of inclined walls, Comput. Methods App. Mech. Eng 191 (47–48) (2002).
[41] J. Eggers, H.A. Stone, Characteristic lengths at moving contact lines for a perfectly wetting fluid: the influence of speed on the dynamic contact angle, J. Fluid Mech. 505 (2004) 309–321.
[42] L.M. Hocking, A moving fluid interface. Part 2: The removal of the force singularity by a slip flow, J. Fluid Mech. 79 (2) (1977) 209–229.
[43] C. Huh, L.E. Scriven, Hydrodynamic model of steady movement of a solid/liquid/fluid contact line, J. Colloid Interface Sci. 35 (1971) 85–101.
[44] R.G. Cox, The dynamics of the spreading of liquids on a solid surface. Part 1. Viscous flow, J. Fluid Mech. 168 (1986) 169–194.
[45] G. Karniadakis, A. Beskok, N. Aluru, Microflows and Nanoflows, Springer, 2005.
[46] E.B.V. Dussan, The moving contact line: the slip boundary condition, J. Fluid Mech. 77 (4) (1976) 665–684.
[47] E. Lauga, P. Brenner, H.A. Stone, Microfluidics: The no-slip boundary condition, in: J. Foss, C. Tropea, A. Yarin (Eds.), Handbook of Experimental Fluid Dynamics, Springer, New-York, 2005.
[48] E. Bänsch, Numerical methods for the instationary Navier–Stokes equations with a free capillary surface, Habilitationsschrift, Albert-Ludwigs-Universität, Freiburg i. Br., 1998.
[49] K. Deckelnick, G. Dziuk, C. Elliott, Computation of geometric partial differential equations and mean curvature flow, Acta Numer. 14 (2005) 139–-232.
[50] G. Dziuk, C. Elliott, Finite element methods for surface pdes, Acta Numer. 22 (2013) 289–396.
[51] S. Turek, Efficient solvers for incompressible flow problems, Lecture Notes in Computational Science and Engineering, vol. 6, Springer-Verlag, Berlin, 1999, http://dx.doi.org/10.1007/978-3-642-58393-3. <http://dx.doi.org/10.1007/978-3-642-58393-3> (an algorithmic and computational approach, With 1 CD-ROM (“Virtual Album”: UNIX/LINUX, Windows, POWERMAC; “FEATFLOW 1.1”: UNIX/LINUX)).
[52] J.W. Barrett, H. Garcke, R. Nürnberg, Eliminating spurious velocities with a stable approximation of incompressible two-phase flow, Tech. Rep. 12, University Regensburg, 2013.
[53] E. Bänsch, Finite element discretization of the Navier–Stokes equations with a free capillary surface, Numer. Math. 88 (2) (2001) 203–235.
[54] V. Girault, P.-A. Raviart, Finite Element Methods for Navier–Stokes equations, Springer Verlag, Berlin, Heidelberg, New York, 1986.
[55] G. Matthies, Finite element methods for free boundary value problems with capillary surfaces (Ph.D. thesis), Otto-von-Guericke-Universität, Fakultät für Mathematik, Magdeburg, 2002.
[56] M.G. Larson, Analysis of adaptive finite element methods (Ph.D. thesis), Department of Applied Mathematics, Chalmers University, Göteberg, Sweden, 1996.
[57] J. Shen, C. Graber, J. Liburdy, D. Pence, V. Narayanan, Simultaneous droplet impingement dynamics and heat transfer on nano-structured surfaces, Exp. Therm. Fluid Sci. 34 (4) (2010) 496–503.
[58] Š. Šikalo, M. Marengo, C. Tropea, E. Ganić, Analysis of impact of droplets on horizontal surfaces, Exp. Therm. Fluid Sci. 25 (7) (2002) 503–510.